Surface slip distributions and geometric complexity of intraplate reverse-faulting earthquakes

Haibin Yang[1], Mark Quigley[1], Tamarah King[1, 2]

Affiliation 1: School of Earth Sciences, University of Melbourne, Victoria, Australia

Affiliation 2: COMET, Department of Earth Sciences, University of Oxford, UK

haibiny@student.unimelb.edu.au

Abstract

Earthquake ground surface ruptures provide insights into faulting mechanics and inform seismic hazard analyses. Surface ruptures for eleven historical (1968 to 2018) moment magnitude (M_w) 4.7 to 6.6 reverse earthquakes in Australia are analyzed using statistical techniques and compared to magnetic, gravity, and stress trajectory datasets. Of the total combined (summative) length of all surface ruptures (~148 km), 133 km (90%) to 145 km (98%) align with geophysical structure in the host basement rocks. Surface rupture length (*SRL*), maximum displacement *(MD)*, and probability of surface rupture at a specified M_w are high compared with equivalent M_w earthquakes globally. This is attributed to (i) steep cratonic crustal strength gradient at shallow depths promoting shallow hypocenters (~1 to 6 km) and limiting down-dip rupture widths (~1 to 8.5 km), and (ii) favorably-aligned crustal anisotropies (e.g., bedrock foliations , faults, fault intersections) that enhance lateral rupture propagation and/or surface displacements. Combined (modeled and observed) *MDs* are in the middle third of the *SRL* with 68% probability, and either the $\leq 33^{rd}$ and $\geq 66^{th}$ percentiles of SRL with 16% probability. *MD* occurs proximate to or directly within zones of enhanced fault geometric complexity (as evidenced from surface ruptures) in 8 of 11 earthquakes (73%). *MD* can be approximated by 3.3 ± 1.6 (1σ) $\times$ *AD* (average displacement). S-transform analysis indicates high-frequency slip maxima also coincide with fault geometric complexities, consistent with stress amplifications and enhanced slip variability due to geometric and kinematic interactions with neighboring faults. Rupture slip taper angles exhibit large variations (-90 % to + 380 % with respect to the

mean value) towards rupture termini and are steepest where ruptures terminate at obliquely-oriented magnetic lineaments and/or lithology changes. Incremental slip approximates *AD* between the 10th and 90th percentiles of the *SRL*. The average static stress drop of the studied earthquakes is 4.8 ± 2.8 MPa. A surface rupture classification scheme in cratonic stable regions is provided to describe the prevailing characteristics of intraplate earthquakes across diverse crustal structural-geophysical settings. New scaling relationships and suggestions for logic tree weights are provided to enhance probabilistic fault displacement hazard analyses for bedrock-dominated intraplate continental regions.

INTRODUCTION

Co-seismic ground surface ruptures on faults provide important sources of information on the seismogenic process (Manighetti et al., 2004; Wesnousky, 2008). Surface rupture characteristics (e.g., maximum displacements (*MD)*; average displacements (*AD);* surface rupture lengths (*SRL)*) may be combined with other seismological parameters to develop earthquake scaling relationships (Allen et al., 2018; Leonard, 2010; Wells and Coppersmith, 1994) for utility in probabilistic seismic hazard analyses (Allen et al., 2018; Stirling et al., 2012) and probabilistic fault displacement hazard analyses (PFDHA) (Moss and Ross, 2011; Youngs et al., 2003).

Slip distributions along surface ruptures are proposed to conform to regular shapes that relate to fracture mechanics, including elliptical shapes (linear elastic theory (Segall and Pollard, 1980)), bell shapes (elastic-plastic theory (Cowie and Scholz,

1992a, b)), or triangular shapes (off-fault damage theory (Manighetti et al., 2004), although heterogenous stress distributions may complicate attribution of rupture shapes to a specific theory (Bürgmann et al., 1994). It is still contested whether co-seismic slip spatial distributions and associated shapes are highly variable or self-similar across different spatiotemporal scales, and what the most probable sources of variability may be (Mai and Beroza, 2002; Manighetti et al., 2009). Although standard simplified shapes (e.g., ellipse or triangle) may enable generalized classification of rupture forms, empirical observations show that many ruptures include embedded hierarchical shapes in wavelength and amplitude that are described as self-similar or self-affine geometries (King, 1983; Power and Tullis, 1991). Fluctuations inside the rupture plane may relate to along-strike variations in the fault roughness (Dolan and Haravitch, 2014; Gold et al., 2015; Perrin et al., 2016; Zinke et al., 2014), the rheology of faulted materials (Haeussler et al., 2004; McGill and Rubin, 1999), fault segmentation (Brown and Scholz, 1985; Klinger, 2010; Manighetti et al., 2009; Okubo and Aki, 1987), fault junctions (Andrews, 1989; Gabrielov et al., 1996; Shen et al., 2009) and/or be attributed to the non-linear, anelastic responses of surficial material to sudden co-seismic strain (Gold et al., 2015; Kaneko and Fialko, 2011; Zielke et al., 2015).

The gradient with which fault slip reduces towards rupture termini (i.e., slip taper) may be linked to the interaction with periphery structures which may directly affect the earthquake arresting dynamics (Manighetti et al., 2004; Scholz and Lawler, 2004). The slip taper is suggested to be a scale-invariant property of rocks (Cowie and Scholz, 1992a, b; Scholz and Lawler, 2004). To discern potential controlling mechanisms of

spatial slip gradient variation for both interior and termini, more detailed field measurements, maps, and analyses of high-resolution co-seismic slip distribution are necessary.

Australian stable continental regions (SCR) comprise non-extended Precambrian crust (Leonard et al., 2014) that is largely unaffected by active tectonic processes relative to plate boundaries and more rapidly deforming intraplate regions (Johnston, 1989). However, Australia SCRs are not immune from seismicity. Since 1968, 11 historical surface-rupturing earthquakes with moment magnitudes (M_w) between 4.7 and 6.6 have occurred in Australian SCRs (Fig. 1A & 1B) (see King et al. (2019) and references therein). These account for more than half of the instrumented global cratonic earthquakes (Clark et al., 2012; Crone et al., 2003). Studies of the source faults suggest long (i.e., $>10^4$ to 10^5 years) preceding periods over which no surface ruptures occurred (Clark et al., 2012), which some workers have interpreted as evidence for 'one-off' rupture behavior on incipient or 'newly formed' brittle faults (Clark et al., 2019; King et al., 2018). Together with the paucity of preceding, historical $M_w > 6$ events on these fault systems (Leonard, 2008; Leonard et al., 2014), this suggests variations in slip rate, interseismic creep, local-to-regional stress perturbations relating to prior earthquake(s), and fault structural maturity (i.e., the roughness of the fault plane, which is physically scaled to $D^{-0.1}$ where D is the cumulative displacement of a fault (Brodsky et al., 2011)) may be of minimal significance to interpreting any slip distribution variability observed in these earthquakes. With the exception of the three surface-rupturing earthquakes on neighboring faults in the 1988 Tennant Creek

sequence, which have been explained by proximate Coulomb stress transfer (Mohammadi et al., 2019), 8 of the 11 Australian ruptures are thus considered to be spatially and temporally isolated, with slip distributions that are unlikely to have been strongly influenced by preceding, spatiotemporally proximate earthquakes.

Issues of data handling and measurement uncertainties have been recently addressed by King et al. (2019), who re-analyzed all Australian surface rupture displacements and established new estimates of net-slip metrics that we utilize here. Driven primarily by exploration needs of the natural resources industry, rich and diverse geophysical datasets have also been acquired and are publicly available across the continent (https://data.gov.au/data/dataset/b0f0711d-9763-4041-9fcf-0b40bd1694a5). King et al. (2019) concluded that 90% of Australian surface-rupturing earthquakes have fault orientations that align with prevailing linear anomalies in geophysical (gravity and magnetic) data and bedrock structure (foliations and/or quartz veins and/or intrusive boundaries and/or pre-existing faults), but did not consider the statistical and scaling relationships of surface rupture displacement fields in detail.

In this study, we propose that the shape of surface rupture displacement profiles and geometric complexity of earthquakes on incipient reverse faults emerging through SCR crust is strongly influenced by the relationships between (i) anisotropic structural and geophysical properties of the host crust that provide potential pathways for seismogenic rupture, (ii) regional stress trajectories that may be locally influenced by geologic variability, and (iii) the depth and dynamics of propagating ruptures that

119 influence how subsurface slip is manifested at the surface. We use net displacements
120 (calculated by trigonometric analyses of vertical and lateral displacements using fault
121 dip estimates) for 10 events from King et al. (2019) and convert surface offsets from
122 the 16th September 2018 M_w 5.3 Lake Muir earthquake (Clark et al., 2019) to net slip
123 assuming pure dip slip and a fault dip of 45°.

124 Rupture data is compared to the national high-resolution (grid cell size ~ 80 m)
125 total magnetic intensity (TMI) map (https://pid.geoscience.gov.au/dataset/ga/89596).
126 Since bedrock is exposed at the surface and/or is only thinly (1 to > 50 m) blanketed by
127 aeolian and/or alluvial sediments (King et al., 2019), TMI signals directly reflect
128 bedrock structures and lithologies in the seismogenic crust. Rock strength properties
129 are not directly measurable by TMI, and we do not attempt to undertake a detailed TMI
130 analysis to resolve three dimensional geometries of TMI anomalies. We focus primarily
131 on the azimuthal relationships between surface ruptures and predominant geophysical
132 structural-lithologic lineaments in the TMI data. The azimuthal relationship between
133 geophysical aspects may reveal rock properties that may affect rupture propagation,
134 e.g., lithological boundaries or fault junctions may have lower frictional strength or
135 modulus than intact rocks (Gabrielov et al., 1996). To locate magnetic anomalies above
136 the source without any distortion, a variable reduction to pole is implemented in this
137 database. Intrusive dikes of relatively lower magnetic susceptibility than host rocks
138 have been detected through aeromagnetic mapping in the Yilgarn craton, where they
139 are characterized by lineament anomalies (Dentith et al., 2009; Dentith et al., 2000).
140 Magnetic lineaments may represent near-vertical structures such as steep faults,

plunging fold axes or intrusive dikes (Dentith et al., 2009), and these features may act as stress concentrators to become the sites of subsequent faulting (Dentith et al., 2009).

To crudely estimate the subsurface position of rupture with respect to anomalies, we assume planar geometries with uniform dip for vertical geophysical structures. Although hypocentral depths are not resolved in high-resolution, most events have centroid moment tensor solutions and/or fault models (e.g. from InSAR) with depths of 1 – 6 km indicating the earthquakes studied herein are sourced from shallow fault ruptures (e.g. King et al. (2019) and references therein). The shallow structures can be tracked as short wave-length responses (magnetic lineaments) in the TMI map. Additionally, national high-resolution gravity data (a grid cell size of ~ 800 m) (https://pid.geoscience.gov.au/dataset/ga/101104) is used to test how the gravitational body forces, which may dominate both the regional and local principal stress direction, might affect rupture complexity. Regional trajectories in maximum horizontal compressive stress (S_{Hmax}) are taken from Rajabi et al. (2017).

GEOLOGICAL SETTING

All historically recorded surface-rupturing earthquakes analyzed here occurred in Australian SCRs (Clark et al., 2012; Leonard et al., 2014) (Fig. 1A). The Archean Yilgarn (Fig. 1A) craton hosted the Meckering (M_w 6.6, 1968), Calingiri (M_w 5.0, 1970) and Cadoux (M_w 6.1, 1979) events in the Southwest Seismic Zone (all earthquakes magnitudes in this paper from Allen et al. (2018)), which is one of the four high-seismicity zones in Australia (Leonard, 2008). The Southwest Seismic Zone (Fig.

1A) also hosted the Katanning (M_w 4.7, 2007) and Lake Muir (M_w 5.3, 2018) earthquakes. The Proterozoic Musgrave block in Central Australia (Fig. 1A) sequentially hosted the Marryat Creek (M_w 5.7, 1986), Pukatja (M_w 5.2, 2012) and Petermann (M_w 6.1, 2016) events. The three Tennant Creek events (Kunayungku M_w 6.2, Lake Surprise West M_w 6.3, Lake Surprise East M_w 6.5, 1988) occurred in the Paleoproterozoic Warramunga Province in the Northern Territory. Geological terrain boundaries are generally not well exposed at the surface but have been inferred from lithological, geochronological, and structure changes (Johnston and Donnellan, 2001); local structures are mapped by detailed geophysical and geological surveys (Fig. 1C). Detailed descriptions of the geological settings of each studied earthquakes are provided in King et al. (2019) and numerous references therein.

OBSERVATIONS

Co-seismic slip distributions and rupture segmentation

Co-seismic net-slip (Fig. 2) is mainly derived from field measurements of vertical and / or lateral discrete surface rupture displacements at surface scarps (Clark et al., 2019; King et al., 2019). Net-slip for Katanning is inferred from InSAR data (Dawson et al., 2008; King et al., 2019). Available displacement data for Lake Muir includes field, UAV and InSAR derived offsets (Clark et al., 2019; Dawson et al., 2008). For this paper we derive net-slip from vertical offsets measured by profiles through InSAR data (Clark et al., 2019), as field/UAV data do not provide full along-rupture coverage.

We investigate the shape of net-slip distributions including the rupture tip taper towards the ends of the faults (termini) and explore the scaling between average displacement (*AD)*, maximum displacement *(MD)*, surface rupture length *(SRL)*, and magnitude (M_w) (Table S1). Since many profiles are not straight lines but rather highly curved, arcuate, and/or segmented, the *SRL* is the sum of different segments and / or linear approximations of the rupture trace (King et al., 2019; Table S1). Segment boundaries were previously assigned where gaps/steps exceed 1 km and/or where fault strike varies by >20° in 1 km (Quigley et al., 2017). For major ruptures with parallel segment ruptures (e.g., Splinter segment in Meckering and the segment in Lake Surprise West), the net slip of each segment is projected and added to its major rupture profile.

Here, we describe a *'fault stepover'* as a location where the most proximate overlapping surface rupture tips are ≥ 100 m apart, as measured normal to the average orientation of the rupture traces (e.g., Petermann; Fig. 1). A '*fault bend*' is a location where a change in fault strike along a continuously mapped surface rupture trace is ≥ 20° (e.g., Pukatja; Fig. 1). A *'fault intersection'* is a location where two faults with distinctly oriented rupture traces intersect at an angle of ≥ 20° (e.g., Meckering, Cadoux, Marryat Creek; Fig. 1). Some locations along a rupture trace may defined as both bends and step-overs (e.g., Calingiri, Pukatja, Fig. 2). Details of slip distributions and rupture segmentation are further described by King et al. (2019).

The Australian earthquake surface rupture patterns are relatively complex when compared with recent global compilations of 135 M_w 4.1 to 8.1 continental earthquakes

205 (Quigley et al., 2017) (Fig. 1D). Rupture complexity is defined by the number of
206 kinematically and structurally-distinct fault segments that ruptured in a 'single
207 earthquake', which is defined as a continuous seismic energy release with no temporal
208 gaps in seismic moment release rate > 20 seconds. An example of how this modifies
209 previous treatment of these data is the 1988 Tennant Creek earthquake sequence (Fig.
210 1C), where multiple mainshocks and surface ruptures were previously amalgamated
211 into a single event (Wells and Coppersmith, 1994; Wesnousky, 2008) despite the
212 earthquakes occurring several hours apart within a 12-hour period and producing
213 independent scarps (Bowman, 1992). Therefore, we treat them as three separate events
214 of M_w = 6.2 (Kunayungku), 6.3 (Lake Surprise West) and 6.5 (Lake Surprise East) with
215 their own surface rupture traces (Mohammadi et al., 2019). Three of those M_w > 5.7
216 events (Cadoux, Meckering, Marryat Creek in Fig. 1D) represent the maximum
217 complexity for corresponding M_w in the global database (Quigley et al., 2017).
218

219 **Shape, symmetry and slip taper of co-seismic slip distributions**

220 To determine whether surface rupture displacement distributions can be well fit by
221 standard shapes (Bürgmann et al., 1994; Manighetti et al., 2004; Segall and Pollard,
222 1980), we fit various regression curves to slip data using the fit function (*fit object*) in
223 the MATLAB curve fitting toolbox
224 (https://www.mathworks.com/products/curvefitting.html). Where large gaps exist
225 between the original observations, we linearly interpolate net-slip between the two

nearest raw data. From this we set a uniform sampling distance of 0.1 km and calculate average displacement (inclusive of interpolated points). Field measurements are coded with grey colors, and interpolated data are coded with red colors in Fig. 2.

Following Wesnousky (2008), we fit offset data using a flat line (i.e., *AD*) and symmetric and asymmetric forms of a triangle and ellipse. For symmetric fittings, the apex (modelled *MD*) is located at the rupture mid-point and is the only free variable. For asymmetric triangle forms, the modelled *MD* and its position are free in regression. For asymmetric ellipse forms, we follow Wesnousky (2008); the shape function is multiplied by a value $(1 - m \times x)$, where x is distance (normalized to rupture length) along the rupture, and m is the variable in regression. The parameter m and the amplitude are two free variables in the asymmetric ellipse function.

We first evaluate goodness of fit using the adjusted R^2, which considers the number of free variables in regression to assess the goodness of fit (Fig. 3A). Adjusted R^2 is correlated with the goodness of fit; $0.5 \leq R^2 \leq 1$ values are crudely considered to represent a good fit of a specified shape function to the empirical displacement data relative to lower R^2. Because R^2 is not a good independent evaluative measure of goodness of fit for horizontal lines, we also use root mean square error (RMSE) normalized to the mean displacement (*AD*) for each earthquake (Fig. 3B), to enhance our statistical comparison amongst earthquakes of different size. Normalized RMSE decreases with increasing goodness of fit (Fig. 3B).

Asymmetric triangle and ellipse shapes ubiquitously exhibit higher R^2 and lower RMSE relative to their symmetric equivalents because they have more allowable free

parameters to enhance the goodness of fit. However, some earthquakes (e.g., Katanning, Kunayungku, Meckering) exhibit high R^2 and low RMSE for all shapes relative to the flat-line *AD* profile ('average' in Fig. 3a, b), with small statistical preference towards asymmetric shapes. Other earthquakes are almost equally poorly fit by symmetric, asymmetric, and *AD* shapes (e.g., Petermann, Lake Surprise West, Lake Surprise East); in these instances, displacement profiles can be generalized by the *AD*. Some earthquakes are statistically poorly fit by most or all shapes (e.g., Cadoux, Pukatja) but are be best represented by asymmetric triangular fits. The Marryat Creek earthquake is approximately equally well fit by asymmetric triangular and elliptical fits.

We further investigate the symmetry of surface rupture displacement profiles by determining the location of the apex of best-fitting asymmetric triangular and elliptical functions (i.e., the modelled *MD*) relative to the normalized surface rupture half-length (Fig. 3C). Importantly, the location and value of the observed *MD* may differ from modelled *MD* (e.g., Calingiri, Lake Muir) as the former may be strongly influenced by changes in fault geometry or interactions, while latter represents a generalized fit to the displacement profile (Fig. 2). Further, if modeled shapes are of low curvature, there may be little significance in the relative position of an apex of the best fit triangle or ellipse along the rupture profile.

We thus refine our definition of rupture symmetry. '*Symmetric ruptures*' contain *MD* within the middle third of the rupture trace (light blue and purple shade, Fig. 2) and have best-fitting shape symmetry ≥ 0.33 in Fig. 3C. Fig. 2 shows n = 8 from observed *MD* (73% of total) and Fig. 3C shows n = 7 (64%) ruptures with best-fitting shape

symmetry ≥ 0.33 (Table S2). The Marryat Creek earthquake is counted in the symmetric category. The most symmetric of these (Kunayunku, Meckering, Lake Surprise East; Table S2) have *MD* in the middle quintile of the rupture trace (light blue shade in Fig. 2 and symmetry ≥ 0.4 in Fig. 3C). *'Asymmetric ruptures'* have *MD* in the end thirds of the rupture trace (Fig. 2; n = 3 observed *MD*) and best-fitting symmetry values of < 0.33 (n = 4; Fig. 3C; Table S2). The most asymmetric ruptures are the Pukatja, Calingiri, and Cadoux earthquakes (Fig. 3C). Collectively, if the two different measures of symmetry are combined, 68% of rupture displacement scenarios are 'symmetric', and 32% are asymmetric, which equates to the probability of a *MD* (observed + modeled) being located in the ≤ 33rd, 33-66th (middle third) and ≥ 66th percentiles of rupture length as 16%, 68%, and 16% respectively.

We also calculate *AD : MD* ratios (Table S1) for each earthquake, for comparison with global datasets (e.g, Wells and Coppersmith (1994); Moss and Ross (2011)). These range from 0.13 (Petermann earthquake) to 0.67 (Katanning) with a mean of 0.38. The relationships between slip at a discrete location along the *SRL* (e.g., for utility in PFDHA) relative to *AD* and rupture displacement shape are explored further in the *Discussion*.

The rupture slip taper describes the gradient of decreasing slip towards the terminus of a fault surface rupture trace (Fig. 3D inset) (Scholz and Lawler, 2004). Asymmetric triangle fits are used to estimate discretized profile-scale slip gradients towards rupture termini. Using these functions enables good fits to be produced for some profiles but may overly smooth the data for some events. This approach

minimizes the over-reliance on individual measurements which may have low signal to noise ratios and misrepresent slip tapers. To refine slip taper estimates for some specific events, we manually fit data using linear regressions to local gradients at rupture termini (thick lines of blue color in Fig. 2), including two termini of the Lake Surprise East event, the right end of Katanning, and the left ends of the Petermann and Cadoux events (Fig. 2 & 3D).

We find an anomalously high value of net-slip 1.5 km from the south termini of the Meckering rupture. We lack confidence in the reliability of the original 1.26 m vertical offset measurement (Gordon and Lewis, 1980) because it is 0.9 – 1.0 m higher than adjacent measurements, and our inspection of SRTM elevation profiles across the projected location of the scarp (http://pid.geoscience.gov.au/dataset/ga/72759) reveals that no scarp of this height is visible (scarp heights of 1 – 2 m are identifiable elsewhere along the rupture). We therefore exclude this measurement from our slip taper calculation but retain it for *AD* estimations as it contributes only ~1% variance to the *AD* estimate and is thus negligible in statistical effect.

Rupture tip taper results are in the range of 2.7 (±1.5) × 10^{-4} (Fig. 3D). Outliers with anomalously steep tapers are the asymmetric Pukatja (right = east end), Lake Surprise East (both ends) and Calingiri (left = south end) ruptures. Since these slip tapers are calculated for individual earthquakes, the estimates can be compared to '*isolated*' and '*interacting*' earthquake tip tapers in the dataset of Scholz and Lawler (2004). The average taper value for the eleven Australian earthquakes studied here (2.7 (±1.5) × 10^{-4}) is consistent with (albeit slightly higher than) the reported average value

of 1.8 (±0.97) × 10^{-4} for '*isolated exterior earthquake tips'* near the end of ruptures that are unlikely to be affected by proximal fault interaction (Scholz and Lawler, 2004). Tip taper outliers from the interacting faults in our study (i.e., the Lake Surprise W and E) are consistent with the Scholz and Lawler (2004) average taper for '*interacting exterior earthquake tips*' of 1.4 (± 1.3) ×10^{-3}.

We acknowledge the tip tapers described here are all from reverse faults, while those in Scholz and Lawler (2004) are from normal-faulting or strike-slip events. The similar taper estimates suggest similar slip taper values may be observed across diverse kinematic modes of rupture and may exhibit scale independence. The prevailing characteristics of surface rupture displacement fields (shape, symmetry, slip tapers) relative to seismological attributes of the associated earthquakes and crustal structure are discussed in more detail in the *Discussion*.

Seismological attributes: epicenter locations, source dimensions, stress drops

We estimate a preferred epicenter location along each rupture profile to determine whether any relationships are evident between probable earthquake nucleation locations and slip distributions (Fig. 2). Earthquake epicenters in Australian SCRs can have large location uncertainties (i.e., $\geq 5-10$ km), particularly for early (pre-1980) and remote events due to the sparse instrumentation of the Australian National Seismograph Network (https://www.fdsn.org/networks/detail/AU/).

Each earthquake studied here has at least three reported epicenter locations. Each reported epicenter is first projected to the nearest surface rupture location; this may be

along the fault trace or a fault tip. Where epicentral locations reside at distances > 15 km from the rupture plane (e.g., the mis-location of initial epicenters for the Marryat Creek earthquake are > 30 km from the rupture plane), these events are excluded from the analysis. Revised locations for epicentral locations are used; for example (Denham, 1988; McCue et al., 1987) favored an epicentral location for the Marryat earthquake on the east-west oriented (W) branch (Fig. 2). We count the number of epicenters that project to each third of the rupture length and consider the rupture third with the most projected epicenters (or best constrained epicenter locations; e.g., we prefer the epicenter locations and associated uncertainties for the Tennant Creek earthquakes using Choy and Bowman (1990)) as the favored host third of the epicenter (horizontal double-arrowed lines in Fig. 2). If the preferred epicenter location is proximal to a boundary between adjacent rupture thirds, we include both thirds as possible hosts for the epicenter. King et al. (2019) present a detailed discussion of the epicenters associated with each earthquake.

The epicenter positions that we display in Fig. 2 are the preferred host third(s) based on all reported epicenter data for each earthquake. A '*unilateral'* rupture (e.g., Katanning, Lake Surprise West, Kunayunku, Cadoux; Table S2) is defined as containing the projected earthquake epicenter in either of the end thirds of the rupture trace, a *'bilateral'* rupture (e.g., Calingiri, Lake Surprise East, Petermann, Meckering; Table S2) contains a projected epicenter in the middle third of the rupture. Where the projected location of the epicenter on to the rupture trace is insufficiently precise to enable designation into a specific third of the rupture (Pukatja, Marryat Creek, Lake

Muir; Table S2), we do not consider it in the analysis of rupture directivity. We do not examine the vertical component of rupture propagation. Of the 8 ruptures analyzed, 50% exhibit unilateral and 50% exhibit bilateral rupture directivity, and no relationship between rupture shape and epicenter location is evidenced.

Hypocenters for all events are subject to large locational uncertainties (> 5 km) due to large distances between the instrumental networks (particularly pre-1980) and earthquake locations (Leonard, 2008). However, revised hypocenter estimates are available for most events (excluding Katanning, Pukatja and Petermann) (Table S4). Additionally, CMT depth results (location of predominant moment release) and modelled faults (e.g. InSAR inversion) are available for some faults (Table S4). These hypocentral, centroid and fault-depth estimates have a combined mean depth of 3.6 ± 1.9 km, while revised hypocenters have mean depths of 4.4 ± 2.1 km. These estimates are significantly shallower than reverse-faulting earthquakes in the non-cratonic areas outside Australia with a mean of 14 ± 5 km (Wells and Coppersmith, 1994; Wesnousky, 2008). We do not consider the contribution of additional (epistemic) uncertainties for this data but note that shallow hypocenters are further required in the Australian examples to balance seismic moments against rupture area constraints.

We estimate down-dip rupture widths (W) by averaging the results of four width estimates (Table S3) based on (a) hypocenter/CMT/fault depths with dip of 45° (b) same depth as (a) with preferred dips from King et al. (2019) (c) revised hypocenters (excl. Katanning, Pukatja and Petermann; see Table S4) with dip of 45° (d) same depth as (c) with preferred dips from King et al. (2019) (all results in Table S5).

379 *SRL:W* ratios are estimated from our preferred widths and shown in Fig. 2 (*SRL* is
380 abbreviated to *L* in Fig. 2). Width (*W)* ranges from 1.2 km (Katanning) to 11.6 km (Lake
381 Surprise East). *SRL:W* ratios range from 0.2 (Pukatja) to 5.5 (Peterman), with an
382 average *SRL*:*W* of 2.4. These are generally consistent with the range of *SRL : W* ratios in
383 global compilations of dip slip earthquakes over the same M_w range (0.7 to 4; average
384 1.5) (Weng and Yang, 2017). *SRL:W* ratios exceed 2.0 in 55% of events. The three
385 earthquakes with longest *SRL* yield the three largest *SRL:W* ratios. The variability in
386 *SRL:W* ratios in this small dataset can be considered high when compared with global
387 data.
388 Stress drops have been reported for several of the earthquakes studied here (Fig. 2
389 caption). It is critical to first acknowledge that stress drops can be estimated via a
390 variety of methods, including (i) static shear stress drop ($\Delta\sigma^s$) from established
391 equations (e.g, Starr (1928)) that include average fault displacements (e.g., ~9 MPa for
392 Meckering and Caligiri; Denham et al. (1980)), and (ii) dynamic stress drops estimated
393 from source time functions (e.g., ca. 5.8 to 13 MPa for the Tennant Creek earthquakes;
394 Choy and Bowman (1990)). Secondly, stress drop estimates are highly sensitive to
395 estimates of rupture size and slip, and variations in fault rock shear strength, and are
396 therefore accompanied by large (and typically uncharacterized) uncertainties both in
397 absolute value and in spatial distribution (Dawson et al., 2008; Denham et al., 1987).
398 Third, stress drops have not been established for all earthquakes studied here and thus
399 there is epistemic uncertainty in how to compare one earthquake with another in this
400 aspect. The highest reported $\Delta\sigma^s$ estimates are 14-27 MPa for the Katanning earthquake

401 (Dawson et al., 2008), and the lowest (ca. 2 MPa) are for the Petermann and Cadoux
402 earthquakes (Attanayake et al., 2020; Denham et al., 1987) (Table S1). Given these
403 uncertainties and variance, ensemble modeling of stress drops using a variety of source
404 fault characteristics and other input parameters is warranted.

405 We model $\Delta\sigma^s$ for all earthquakes by averaging the results from four stress drop
406 estimates which include: the method from Madariaga (1977) using seismic moment M_O
407 (estimated from M_W), W, and fault area (assuming an elliptical fault); the method of
408 (Griffith et al., 2009) based on Madariaga (1977) using AD, W, L, with 20 GPa and 50
409 GPa shear modulus (μ) (Zhao and Muller, 2003); and published stress drops (Table S1).
410 The full results of these estimates are detailed in Table S6 and Figures S1 and S2.

411 Our $\Delta\sigma^s$ range from 1.5 ± 0.9 MPa (Marryat Creek) to 9.5 ± 5.9 MPa (Lake
412 Surprise West) with a mean of 4.8 ± 2.8 (1 σ) MPa. These vary from previously reported
413 $\Delta\sigma^s$ (Table S1) by 21 % (Cadoux) to 56% (Katanning) (note that our calculations
414 incorporate these previously published data).

415 Cratonic *in situ* stresses have relevance to discussions on the seismological
416 characteristics of these earthquakes. Proxy measurements of stresses at 0 to 1.5 km
417 depth (extrapolation to greater depths) imply large increases in maximum horizontal
418 and deviatoric stresses from the surface (ca. 5 to 20 MPa), to ca. 1.5 km depth (ca. 100
419 MPa; Bamford (1976)) and to depths of ca. 5 km (ca. >200 MPa; Denham et al. (1980)).
420 The possibility that stress drops exhibit an aspect of depth-dependence is considered in
421 this context (Huang et al., 2017).

422

S-transform analysis of the slip residuals

Earthquake slip distributions commonly exhibit aspects of hierarchical self-similarity or self-affinity (Frankel, 1991; King, 1983; Mai and Beroza, 2002) that manifest as low amplitude and short wavelength features (i.e., low level shapes) embedded into the high amplitude and long wavelength first-order shape of the total displacement field (i.e., the basic shape).

To investigate the spectral characteristics and distributions of low level shapes, we first subtract the basic shape component from the discrete observations and apply S-transform analyses on the residuals (Stockwell et al., 1996). The basic shape (triangle or ellipse) is selected by the shape fitting with higher R^2 (Fig. 2). The S-transform is based on the idea of the continuous wavelet transform and has a moving and scalable localizing Gaussian window. The advantage of the S-transform is that it can deal with non-stationary signals (like the slip distributions in this study), and provide a clear space-frequency representation of the slip distribution, which is not available for the classical Fourier spectrum method.

The S-transform given by Stockwell et al. (1996) is expressed as $S(l,k) = \int_{-\infty}^{\infty} h(x) \frac{|k|}{\sqrt{2\pi}} e^{-(l-x)^2 k^2} e^{-i2\pi kx}\, dx$, where S is the S-transform of the space function $h(x)$, which is the residual spatial distribution; k is the spatial frequency and l is the parameter which determines the position of the Gaussian window. The window size is inversely scaled with k. The S-transform characterizes the local spectrum, and averaging the local spectra over the whole space gives the Fourier spectrum as $\int_{-\infty}^{\infty} S(l,k)dl = H(k)$, where $H(k)$ is the Fourier transform of $h(x)$. In this study,

$h(x)$ of each event is normalized by the corresponding maximum residual. In the following, we first demonstrate the frequency-space distribution, $S(l,k)$, of the residual signals, and then check its averaging representations, $H(k)$. A potential source of sampling bias is that some fault segments have fewer measurements relative to others, and that the slip shapes derived for the faults with sparse measurement data may be oversimplified.

Fig. 4 shows the results of the S-transform analysis. The spatial frequency parameter k is a discretized value of *SRL* / the wavelength of the specified increment. For example, a value of k = 50 is equal to a wavelength of 280 m for the Marryat Creek earthquake (*SRL* = 14 km) and 780 m for the Meckering earthquake (*SRL* = 39 km). A value of k = 0 represents a rupture shape wavelength >1.5 *SRL* with an infinite upper limit representing a horizontal line (i.e., residuals that are collectively fit by a shape with a wavelength longer than *SRL*). A value of k = 1 is equivalent to fitting the displacement profile with one shape (wavelength = *SRL*). As the uniform resampling interval is 100 m, the highest spatial frequency that can be recovered is 200 m. The z axis is a unitless measure of the relative apportionment of energy (i.e., probability distributions) for different residual wavelengths (i.e., spatial frequencies) plotted as discrete (100m) increments along the *SRL*. Since the range of computable values for k is conditional upon *SRL* and the minimum wavelength of the sampling interval, larger values of k can be estimated for longer ruptures (e.g., Meckering, Petermann) relative to short ones (e.g., Pukatja, Calingiri).

Fig. 5 shows the averaged S-transform results *H(k)* over the whole rupture length

467 (Table S2). The Pukatja earthquake exhibits minimal statistical preference amongst k
468 =1 to 4. This is consistent with (i) the highly sinuous and structurally complex surface
469 rupture morphology that could promote slip variability (manifested as embedded
470 shorter wavelength shapes in the general profile), and (ii) the high density of surface
471 displacement measurements, that could enhance recognition of any displacement
472 variability (Clark et al., 2014). Enhanced high frequency energy at $4 \geq k \geq 8$ in the
473 eastern third of the rupture is associated with the location of peak displacement and
474 variability at a step-over (Fig. 1, 4).

475 The Katanning earthquake exhibits clear statistical preference for k =1 with small
476 signals associated with k = 0 (suggestive of adherence to a broader form) and k = 2
477 and 3 towards rupture termini (Fig. 4), where small fault orientation changes are
478 possible based on InSAR data (Fig. 1) (Dawson et al., 2008) and where enhanced
479 variability would be expected as deformation is diffused from the primary fault. This
480 earthquake exhibits the simplest S-transform spectra and is consistent with a shallow
481 focus, circle-shaped, structurally simple rupture (Dawson et al., 2008) although these
482 data also reflect our utility of the INSAR-derived rupture model, given the lack of
483 discrete field-observed surface displacements.

484 The Calingiri earthquake exhibits a statistical preference for k = 3 (and k = 2)
485 above k = 1, consistent with the segmented rupture trace (Fig. 1) and deformation
486 undulations at wavelengths of ~1.3 to 2 km (Fig. 2, 5B). The zone of enhanced high
487 frequency energy ($8 \leq k \leq 15$ corresponding to wavelengths of 500 to 260 m; Fig. 4,
488 5B) is concentrated in the southern half of the rupture and is coincident with

maximum displacement at a fault stepover (Fig. 2, 4).

The Lake Muir earthquake exhibits statistical preference for k = 2 (and k = 3) corresponding to wavelengths of 2.4 (and 3.6 km). The preference of a segmented rupture is consistent with distinctive trends in the rupture trace with ~20 to 45^{o} variance (Clark et al., 2019). Embedded shorter wavelength triangular shapes (Fig. 2) are identified at $6 \leq k \leq 9$ (1.2 to 0.8 km wavelength) (Fig. 4, 5A, 5B) and these include additional hierarchies of embedded energy undulations at higher k (Fig. 4). High frequency energy signals coincide with peak displacement at a small fault step-over, and change in average rupture trace orientation (fault bend), in the eastern half of the rupture (Clark et al., 2019) (Fig. 1, 2).

The source ruptures of the 1988 Tennant Creek share similar attributes: *(i)* a clear statistical preference for low k (k = 1 for Lake Surprise W and E; k = 2 for Kunayungku), with progressively decreasing contributions with increasing k (particularly distinct when compared to the similarly-sized Marryat Creek and Petermann earthquakes; Fig. 4, 5A, 5B), *(ii)* localized pulses of energy at high k in the central portions of rupture traces (all), coincident with peak displacements that may be associated with fault bends +/- intersections (Lake Surprise E) (Fig. 1, 4), and *(iii)* minimal energy contributions from wavelengths < 3 km (Fig. 5B). In comparison, the Marryat Creek and Petermann earthquakes are characterized by *(i)* large mean energy contributions at $k \geq 5$ in Fig. 5A (wavelength ~ 2-3 km) that are similar to the mean relative probabilities at k =1 or 2 (Fig. 5A), and *(ii)* localized high k (> 10) peaks (~ 1 km wavelengths; Fig. 4) coincident with maximum displacement domains at fault

intersections (Marryat Creek) and step-overs (Petermann) (Fig. 1, 2). In addition to the distinctions, it is notable that the Lake Surprise E and W, and Petermann earthquakes exhibit less definitive shape profiles that are as almost as well represented by average displacements (flat lines) as triangular or elliptical fits, whereas Kunayungku and Marryat Creek adhere more closely to asymmetric triangles.

The Cadoux earthquake is statistically best-defined by a single (k = 1) asymmetric triangle displacement profile (Fig. 2, 4, 5) despite a highly complex and segmented (n= 6 faults; King et al. (2019)) rupture trace (Fig. 1), suggesting strong transfer of vertical displacement across complex fracture networks. Both the northern and southern thirds of the rupture include local slip maxima at high-angle fault intersections (Fig. 1, 2) and high k spikes associated with embedded high frequency triangular shapes (Fig. 2). Distinct from Lake Surprise W and Kunayungku, there is a persistent mean probability signal at $2 \geq k \geq 10$ (Fig. 5); the upper range (k = 5 to 10) of which corresponds with wavelengths of 4.6 to 2.3 km.

For the Meckering earthquake we analyze the full published dataset, without removing the anomalously high net-slip value previous discussed in the southern part of the rupture. The Meckering earthquake exhibits consistent relative probabilities for k =1 and k = 2, both of which are statistically preference in the $0 \geq k \geq 10$ range (Fig. 5). A high k spike is observed at the southernmost end of the rupture (Fig. 4). The persistent signal at $4 \geq k \geq 10$ (Fig. 5A, 5B) corresponds to contributions from ~9.8 to 3.9 km wavelengths; these are evident as hierarchical, self-similar triangle-shaped features embedded within the overall triangular-shaped slip shape (Fig. 2). The

533 Meckering earthquake could have comprised as many as 4 to 8 planar faults (Fig. 1D);
534 consistent with elevated signals at $k \geq 4$. No evidence for fault trace orientation
535 changes or fault intersections on displacements is found; the displacement profile is
536 statistically well fit by the triangular shape function (Fig. 3).

537 ***MD*, *SRL*, and fault geometry**

538 We plot *MD* and *SRL* against M_w (Fig. 6) and compare against global thrust fault
539 regressions from Wells and Coppersmith (1994) and Moss and Ross (2011). The 1989
540 Ungava, Canada earthquake (Adams et al., 1991) also occurred in a non-extended
541 craton and is included with the Australian events for our linear regression analysis.
542 Regression equations are given in Fig. 6. For events of $M_w < 7$, the linear regression
543 fitting shows that both the *MD* and *SRL* in non-extended cratonic areas are higher than
544 global comparatives (Fig. 6). The large *SRL* for SCR earthquakes compared to
545 analogous M_w global earthquakes is also reported by Clark et al. (2014).
546 Wells and Coppersmith (1994) found that the *SRL* is typically about 75% of
547 subsurface rupture length. However, balancing M_w against *AD*, *L*, and shallow
548 down-dip rupture width (i.e., rupture area), and considering aftershock distributions
549 with respect to *SRL*, suggests *SRL* ≈ subsurface rupture length in the Australian SCR
550 earthquakes studied here. For example, the precisely located aftershocks of the
551 Petermann earthquake enable mapping of a maximum sub-surface rupture length that is
552 ≈ *SRL* (Attanayake et al., 2020). This may be attributed to the shallow earthquake
553 ruptures in bedrock that extend to the surface without significant influence of thin

554 sediments.

555 Following our descriptions of fault stepovers, bends, and intersections above, we
556 compare the locations of observed *MD* against these fault geometric aspects. *MD* for
557 the Petermann coincides with a fault stepover (Fig. 1, 2). *MD* for Pukatja, Lake Surprise
558 East, Calingiri, Cadoux, and Lake Muir coincides with fault bends (Fig. 1, 2) and in the
559 case of Pukatja and Calingiri, small step-overs in the rupture trace. *MD* for Meckering,
560 and Marryat Creek coincides with fault intersections (Fig. 1, 2). Fault geometries in the
561 regions of *MD* on the Kunayungku, Lake Surprise West, and Katanning surface
562 ruptures can be considered sufficiently homogenous to not require classification into
563 the geometric categories described above. In summary, *MD* occurs proximate to or
564 directly within zones of enhanced fault geometric complexity (as evidenced from
565 surface ruptures) in 8 of 11 earthquakes (73%), and *MD* can be approximated by 3.3 ±
566 1.6 (1σ) × *AD*.

567

568 **Probability distribution of co-seismic slip**

569 The probability distribution of co-seismic slip is suggested to be a proxy of stress
570 distribution and fault strength by Thingbaijam and Mai (2016), who undertook
571 probability analysis by using sub-surface co-seismic slip data. Due to the limited
572 dataset of surface co-seismic slip, especially for those earthquakes of $M_w < 6$, we only
573 analyze the probability distribution of co-seismic slip for two endmember cases of
574 Meckering and Petermann, for which the surface rupture geometry shows significant

differences in distribution and shape (Fig. 1, 2).

With the uniformly sampled (0.1 km) co-seismic slip data, we first count the bins of slip value in corresponding ranges; then measure the complementary cumulative distribution function ($1 - F(u)$), which is fit by the exponential function, $e^{(-u/u_h)}$, and the truncated exponential function, $\frac{e^{(-u/u_c)} - e^{(-u_{max}/u_c)}}{1 - e^{(-u_{max}/u_c)}}$, where u and u_{max} are the co-seismic slip and the maximum slip, respectively; u_h and u_c are the unknown rate parameters used in the regression for exponential function and truncated exponential function, respectively. In the case of the truncated exponential function, we also define u_t which denotes the position where the probabilities start to deviate from an exponential trend (Fig. 7). Both u_h and u_c are related to the expected value of the distribution, but u_c is likely to be larger than the maxima of the distribution, and the physical implications of different u_c is discussed later. The goodness of fit is measured by R^2.

The Meckering event is best fit by the truncated exponential function, while the R^2 is the same for both fitting functions in the case of Petermann earthquake (Fig. 7). The Meckering and Petermann cases represent two endmember cases listed in Thingbaijam and Mai (2016): $u_c > u_t$ (subcritical behavior in Meckering where u_c is larger than the u_{max}, thus not shown in Fig. 7B) and $u_c < u_t \approx u_{max}$ (near-critical behavior in Petermann where u_t is close to u_{max}, thus both fitting function produce close R^2). These end members describe fault rupture propagation that has to overcome strong physical constraints during rupture (subcritical) versus weak physical impediments to rupture (near-critical).

The subcritical behavior observed for the Meckering event is suggestive of a spatially variable co-seismic stress drop (including relatively high and low components) due to rupture on crustal structures that are variably-oriented with respect to S_{Hmax} (Fig. 1, 8) and that require complex kinematic and geometric interactions to enable rupture propagation. This may ultimately favor a triangular shape for the slip distribution. Conversely, in the Petermann earthquake, the relatively straight, simple and 'weak' source fault (related to inherited bedrock structure) and high-angle relationship with respect to S_{Hmax} and gravity gradient, may favor a more uniform displacement (low curvature) shape, albeit with localized complexity at a fault step-over (Fig. 1).

Comparison of rupture orientations with crustal geophysical properties

Surface rupture traces are plotted on aeromagnetic intensity maps in Fig. 8 and on Bouguer gravity contour maps in Fig. 9. Additional rupture characteristics (stress drops $\Delta\sigma^s$, discretized surface rupture orientations with respect to S_{Hmax}) are shown in Fig. 10 and compared to geophysical setting below.

All earthquakes similarly exhibit rupture traces that clearly align with prevailing magnetic structures (King et al., 2019). The Petermann earthquake surface rupture parallels the predominant NW-trending orientation of regional magnetic structure (Fig. 8) and is parallel to NW-striking, NE-dipping bedrock foliations at the surface (Attanayake et al., 2020; King et al., 2019). Magnetic fabrics continue in rupture-parallel orientations beyond the rupture termini, although minor curvature is

618 evident at the NW end; no high angle geophysical structures that could act as barriers to
619 rupture are identified. The Pukatja surface rupture trace parallels the edge of a strong
620 magnetic contrast. The Marryat Creek ruptures are sub-parallel to E-W and
621 NNE-trending lineament sets. The three Tennant Creek ruptures parallel NW and ~E-W
622 lineaments, geological contacts, and previously mapped faults (Fig. 1C). The complex
623 array of surface rupture traces in Cadoux parallel NW, NE, and E-W to ENE-WSW
624 oriented magnetic fabrics. The northern and southern sections of the Meckering rupture
625 parallel NE and NW-trending magnetic lineaments respectively; the central N-S
626 striking rupture coincides with a less well defined but still identifiable zone of changes
627 in magnetic structure and intensity. Katanning parallels NE-trending lineaments. The
628 Calingiri rupture parallels N-trending lineaments (Fig. 8). Clark et al. (2019) conclude
629 that the Lake Muir rupture trace parallels pre-existing structures evident as N to
630 NE-trending surface features (valleys) that parallel minor lineament trends in the
631 magnetic data; the bedrock structural controls on Lake Muir are amongst the least
632 obvious in our dataset.

633 Of the total combined (summative) length of all surface ruptures (~148 km) we
634 estimate between 133 km (90%) and 145 km (98%) aligns with geophysical structure in
635 the host basement rocks (Fig. 8). In instances where one orientation of magnetic fabric
636 is clearly dominant in the host bedrock (e.g., Petermann, southern part of Marryat
637 Creek, all Tennant Creek earthquakes) the entire rupture trace is parallel to that fabric.
638 Where two or three sets of magnetic fabrics are present, ruptures may involve all fabrics
639 (e.g., Marryat Creek, Cadoux, Meckering) or remain confined to a single trace that is

parallel to one fabric and truncated by distinct high-angle fabrics (e.g., Katanning, Calingiri).

Type classification scheme for earthquakes based on crustal structure and rupture characteristics

Type 1

The straightest (i.e., smallest range in incremental orientations; Fig. 10A; classified as "*Type 1*" ruptures) and least segmented ruptures are the Petermann, Kunayungku, and Lake Surprise East ruptures. These *Type 1* ruptures all share the following characteristics: (1) the host bedrock contains a dominant bedrock fabric (e.g., penetrative TMI fabric, surface geology foliations and faults) that is structurally continuous on the scale of surface ruptures (e.g., 10's of km) and oriented perpendicular-to-high angle with respect to gravity gradients and S_{Hmax}; (2) the average surface rupture trace is oriented approximately parallel to this bedrock fabric; (3) surface rupture traces have the lowest range of S_{Hmax} relative orientations (~28° to 52° from S_{Hmax} perpendicular; Fig. 10B and inset) and are all oriented approximately perpendicular to the gravity gradient; (4) mean $\Delta\sigma^{s}$ derived from ensemble models are average (e.g., Lake Surprise East) to low (e.g., Petermann) relative to the average from all earthquakes (Fig. 10A); (5) observed *MD* is in the central third of the ruptures (Fig. 2); and (6) modeled displacement shapes are symmetric and lower amplitude, with a preference for elliptical shapes with centrally-located, modeled *MD* (ellipse apices, Fig. 2) of similar value to *AD* (excluding Kunayungku).

662 The Petermann earthquake surface rupture is an example of *Type 1* earthquake. The
663 rupture orientation is relatively straight (Fig. 10B) and oriented between 27 to 47^{o}
664 (clockwise) from the normal of S_{Hmax} (Fig. 8). With a dip of ~30^{o} (Attanayake et al.,
665 2020), the fault is thus well oriented for reverse-oblique faulting. The rupture source
666 can be generally described as a fault that is sub-parallel to micaceous foliations in the
667 hosting bedrock. Bedrock fabrics and the rupture trend between 30 – 45° from S_{Hmax}
668 perpendicular (Rajabi et al., 2017). Parallelism with bedrock fabrics is suggested to
669 have enhanced rupture gliding and promoted a low stress drop rupture (Attanayake et
670 al., 2020). The modeled *MD* for triangular and elliptical shapes is similar to the *AD*
671 (although the observed *MD* is ~ 7 *AD*; Fig. 2). The critical behavior of the Petermann
672 event observed in our probability distribution analysis of co-seismic slip indicates that
673 this event had a relatively weak fault strength which results in a low amplitude elliptical
674 to *AD* slip distribution. The rupture trace is orthogonal to the regional gravity gradient
675 (Fig. 9) and thus stress perturbations that could result from geological density contrasts
676 could enhance the propensity towards reverse slip. The mean $\Delta\sigma^{s}$ derived from
677 ensemble models of the Petermann earthquake (Table S1) is 2.7 ± 1.0 (1 σ) MPa; this is
678 lower than the average $\Delta\sigma^{s}$ from all earthquakes and is low compared to median stress
679 drops from intraplate earthquakes globally (~ 6 MPa; Allmann and Shearer (2009)).
680
681 *Type 2*
682 *Type 2* crust contains multiple intersecting bedrock fabrics with varying
683 orientations with respect to S_{Hmax} and gravity gradients, and no clearly dominant

684 bedrock fabric at the scale of the individual rupture traces. *Type 2* ruptures (Katanning,
685 Calingiri, Lake Surprise West, Marryat Creek, Pukatja, Meckering) exhibit surface
686 rupture complexity, as evidenced by a large range of orientations relative to the
687 perpendicular of S_{Hmax} (0° – 80°) and numerous stepped profiles in the cumulative *SRL*
688 plot (Fig. 10B; Table S9). Highly misoriented (i.e., all traces >45 to 60^{o} with respect to
689 the perpendicular of S_{Hmax}) *Type 2* ruptures that are also influenced by surrounding
690 high-angle structures (e.g., Lake Surprise W is bounded by Lake Surprise E and
691 Kunayungku; Katanning is bounded by high angle geophysical lineaments; Fig. 8)
692 exhibit the highest mean $\Delta\sigma^{s}$ (Fig. 10A). Due to the high structural complexity of *Type*
693 *2* crust, *Type 2* ruptures exhibit the largest range in $\Delta\sigma^{s}$, including the lowest $\Delta\sigma^{s}$ event
694 (Marryat Creek; Fig. 10A), and the greatest diversity in orientations with respect to
695 S_{Hmax} (e.g., Calingiri vs. Lake Surprise West).
696
697 *Type 3*
698 *Type 3* crust (locations of Lake Muir and Cadoux earthquakes) contains a
699 dominant bedrock structure that is highly misaligned (i.e. < 20°) to S_{Hmax} and thus
700 unfavorable for earthquake ruptures under the stress regime (see black arrows and
701 dashed lineaments for Lake Muir and Cadoux in Fig. 8). Secondary structures include
702 inherited faults and foliations that may be favorably or unfavorably oriented for brittle
703 slip within active stress field. Gravity gradients may be highly oblique to S_{Hmax} (Fig.
704 9). Surface rupture geometries may be highly complex and variably oriented,
705 particularly the Cadoux earthquake (Fig. 1, 10B); rupture traces tend to be more

706 bimodally distributed into optimally (0-10^{o}; Fig. 10B) and highly misoriented (> 60^{o};
707 Fig. 10B) segments that reflect the interplay between extrinsic forcing by regional S_{Hmax}
708 and the (misoriented) intrinsic structural properties of the host crust. This rupture type
709 also exhibits the highest overall degree of asymmetry in both modeled and observed
710 *MD*. The preferred rupture shape is triangular, which we attribute to an increased
711 distribution of off-fault damage associated with rupture propagation through
712 structurally unfavorable host rock. Both *Type 3* events considered here are shallow,
713 with very large *SRL*:*W* ratios (Fig. 2) and relatively low $\Delta\sigma^{s}$ (Fig. 10A).

714 In terms of the Cadoux earthquake, the southern half of the surface rupture is
715 primarily N-S oriented and well aligned with respect to S_{Hmax} for reverse faulting, while
716 the northern half consists of a complex array of short E-W and N-S oriented rupture
717 segments (Fig. 8). We posit this change in structural complexity may primarily reflect
718 two aspects: (i) increasing abundance of misoriented penetrative E-W oriented
719 structures to the north, which disrupt the N-S rupture and transfer slip across the
720 complex fault array, and (ii) increasing influence of a large volume positive Bouguer
721 anomaly to the north (indicated by circular contours in Fig. 9; also coincident with a
722 zone of higher magnetic susceptibility on the TMI image in Fig. 8) that imparts a N-S
723 gravity gradient that is approximately parallel to the average rupture trace orientation
724 and is at a high angle to S_{Hmax}. We suggest the latter effects locally increase the
725 proportional contribution of the secondary horizontal stress (σ2) relative to the regional
726 S_{Hmax} (σ1), therein increasing the potential for rupture transfer on to higher angle faults
727 and overall rupture complexity. Local stress field rotations, including the possibility

728 that the magnitude of the N-S oriented compressive stress locally exceeds the regional
729 S_{Hmax}, remain plausible hypotheses, collectively highlighting the potential for crustal
730 structure to impart significant influence on rupture complexity. The slip asymmetry,
731 with *MD* towards the rupture terminus (Fig. 2), poor statistical fit to all functions and
732 highly variable slip tapers at either end of the rupture (Fig. 3), abundant higher
733 frequency displacement energy with embedded triangular slip shapes (Fig. 2, 4, 5) are
734 additional characteristics of this rupture type.
735

736 **DISCUSSION**

737 **High-frequency slip maxima**

738 S-transform analysis reveals high-frequency (k > 10) signals in four events that
739 are spatially coincident with high spatial slip gradients (> 10^{-3}) at fault stepovers
740 (Petermann), bends (Calingiri, Lake Surprise East), and fault intersections (Cadoux).
741 Stepover widths on all faults are ubiquitously less than 2 km, consistent with
742 empirical evidence for rupture propagation across < 2 km-wide stepovers (Wesnousky,
743 2006, 2008).

744 For a *Type 1* rupture like Petermann, we suggest the observed high slip gradients
745 and high-frequency signals at the steps are related to highly dynamic stress
746 concentrations associated with rupture propagation across neighboring fault segments
747 (Elliott et al., 2009; Oglesby, 2008). The threshold value of spatial slip gradient that
748 permits rupture jump over gaps and stepovers was suggested to be > 2×10^{-4}, which

749 was based on the analysis of continental strike-slip earthquakes (Elliott et al., 2009).
750 The observed spatial slip gradient in the Australian examples studied here is about one
751 order of magnitude higher than the threshold value.

752 We note that the high slip gradient is only one aspect of the high-frequency
753 signals; an abrupt increase and decrease of slip within several hundred meters is also
754 observed. This short-wavelength feature is not predicted in the high stress
755 concentration model (Elliott et al., 2009; Oglesby, 2008) nor the theory of shallowly
756 connected faults (Oglesby, 2020). It may relate to short-wavelength geological
757 anomalies with lower shear modulus relating to lithologies that are cut by the fault
758 (Bürgmann et al., 1994) or shallowly connected fault segments (e.g., en-echelon
759 fracture networks) only hundreds of meters long (Oglesby, 2020; Quigley et al., 2012).
760 However, we do not find any evidence of lower shear modulus materials or short fault
761 segments for these ruptures, based on examinations of geological and rupture maps,
762 except for Cadoux (see next).

763 Zones of geometrically complicated interacting faults connected by opening
764 fractures have been found elsewhere to produce the comparable high-frequency signal
765 features to those observed here (e.g., see Fig. 9 in Bürgmann et al. (1994)). The
766 linking fractures are able to transfer slip efficiently (Bürgmann et al., 1994). Fractures
767 connecting fault bends and intersections were identified at Cadoux and Calingiri
768 (Gordon and Lewis, 1980; Lewis et al., 1981). The high-frequency signal in Marryat
769 Creek is correlated to the fault junction zone where intersecting faults are
770 orthogonally oriented with a wedge-shaped rupture geometry that can be considered

kinematically and geometrically compatible. The mechanics of fault junctions suggests the intersection of these types of faults could act as earthquake nucleation points and foci of maximum slip (Andrews, 1989). If fault steps, bends, or high-angle fault intersections act as kinematic asperities, we might anticipate these to coincide with slip maxima associated with maximum seismic energy release, and also high frequency variations in slip as variations in the intrinsic characteristics of the fault zone influence the dynamics of the propagating rupture.

Slip taper and barriers

Here we focus on the four events with slip taper > 10^{-3} that are considered outliers in Fig. 3D. The high rupture tip taper value has been attributed elsewhere to (1) off-fault barriers of high frictional strength, (2) blocks of reduced shear modulus, (3) obliquely oriented structures, and (4) rupturing into a fault region that has previously experienced a large earthquake and is at a residual stress state (Cappa et al., 2014; Manighetti et al., 2004; Perrin et al., 2016; Scholz and Lawler, 2004). The faults in Australian cratonic regions are considered immature or incipient faults (following definitions from (Brodsky et al., 2011; Perrin et al., 2016). An absence of scarps in proximity to these historic ruptures suggests (4) is unlikely to account for the observed displacement patterns (Clark et al., 2019; Clark and McCue, 2003; Crone et al., 2003).

In this section, detailed structures are described for each surface-rupturing earthquake. The Calingiri event is asymmetric in slip distribution with a high rupture tip taper (1.2×10^{-3}) at the southern tip (Fig. 3D; left end in Fig. 2). The southern tip is

792 found to terminate at a nearly north-south striking lineament of low magnetic anomaly
793 (dashed purple line in Fig. 8), while the whole rupture extends into a high-anomaly
794 body, which sits on the hanging wall (Fig. 8).

795 The Pukatja event is 1.6 km long and has an asymmetric slip distribution with a
796 high rupture tip taper value (2.9×10^{-3}) at the eastern tip (Fig. 3D; right end in Fig. 2).
797 The eastern tip stops at a lineament of high magnetic susceptibility while the other end
798 (west) cuts into a body of relatively lower susceptibility (dash purple line in Fig. 8). The
799 ends of other rupture tips of normal taper values (Fig. 3D) are not found to stop
800 coincident with lineaments like those cases of high rupture tip taper values (Fig. 8).

801 The relatively high rupture tip taper in the right end (east) of Lake Surprise W and
802 the left end (west) of Lake Surprise E (Fig. 3D) may be explained by the abrupt change
803 of the dip direction of the hosting reverse fault (Fig. 1C) (Bowman, 1992; Mohammadi
804 et al., 2019). The Lake Surprise W event ruptured a NE-dipping fault while the Lake
805 Surprise E event ruptured a SW-dipping fault (Fig. 1B, 1C) (Bowman, 1992). For the
806 high rupture tip taper of the right tip (east) of the Lake Surprise E event, referring to the
807 1:250,000 Tennant Creek interpreted basement geology map (Johnston and Donnellan,
808 2001), we find it stops at a location coincident with a fault separating volcanoclastic
809 units from the undifferentiated granite (Fig. 1C).

810 These observations collectively suggest that obliquely orientated bedrock
811 structures, identifiable as magnetic lineaments in geophysical data, coincide with the
812 termini of some of the ruptures studied here, and can are associated with anonymously
813 steep rupture tip tapers. No clear relationship is observed between tip taper steepness

and prevailing rupture directivity, as proxied from estimates of epicentral location (Fig. 2). The relationship between high rupture tip taper value and the presence of magnetic lineaments at high angles to the rupture plane provides evidence that obliquely oriented bedrock structures may be effective barriers to rupture propagation. Lineaments orientated unfavorably to the rupture propagation direction may channel the propagating rupture into less efficient fracture pathways, therein dissipating fracture energy and terminating rupture propagation.

Through the study of structural control on rupture tip taper and the complexity of rupture segmentation, the role of pre-existing structures in facilitating or stopping rupture development is evident. The concept of rupture potential may provide some hint to the relations between earthquake initiation point and terminus point (Weng and Ampuero, 2019). The rupture potential theory suggests that final rupture termini are located at the places of the same rupture potential as that at the initiating position. The rupture potential theory determines the potential size of an earthquake provided that the spatial distribution of G_c/G_0 is obtained, where G_c and G_0 are the fracture energy and the steady state energy release rate, respectively. The fracture energy is a function of rupture acceleration, which is not available before the earthquake occurs, and may be obtained from some physical scaling, thus introducing large uncertainties.

Applying this theory to the Australian cratonic earthquakes, we find that where an initiating point is in the intersecting part of two faults, which had a high rupture potential, the earthquake would rupture through other intersecting segments. This forms complex rupture patterns as seen for the Meckering, Lake Muir, and Marryat

836 Creek events. If the events initiated between two lineaments (dashed purple lines in
837 Fig. 8) and was of lower rupture potential than that of the intersection points, the final
838 rupture would be limited by two lineaments. This forms relatively simple rupture
839 patterns, like the Pukatja and Katanning events, where ruptures are located between
840 two large magnetic lineaments (dashed purple lines in Fig. 8). Therefore, the potential
841 rupture length of a weak zone that is normal to the S_{Hmax} is controlled by two
842 intersecting segments and is determined by the rupture potential of the initiating point.
843 In addition, the geophysical heterogeneity derived from the gravity map may
844 reveal controlling factors on the Petermann earthquake, where no intersecting
845 structure is detected through the TMI map. The gravity contours (marked by thick red
846 lines in Fig. 9), to the north-east of the surface rupture of the Petermann event,
847 demonstrates a sudden offset (at the position P and P' in Fig. 9) from the general trend
848 where it is coincident with the location of the rupture, which is dipping to the NE.
849 This sudden change of gravity contours reflects a shallow high-density anomaly
850 beneath the surface (Fig. 9). The size of this anomaly is comparable to the surface
851 rupture length and may have controlled the length of the final rupture.

852 **Scaling between *MD*, *SRL* and *Mw***

853 Fig. 6 demonstrates that Australian cratonic earthquakes have larger *MD* and
854 longer *SRL* than other earthquakes of comparable M_w (Wells and Coppersmith, 1994),
855 with a few exceptions (e.g., Pukatja, Tennant Creek earthquakes in *SRL*). The
856 Australian earthquakes also predominate the subset of the global data with hypocenters

857 shallower than 7 km depth (filled symbols). We note that the small sample size limits
858 our confidence in whether the earthquakes studied here represent the expected range of
859 surface-rupturing earthquake behaviours in cold and stable cratonic crust and we
860 cannot dismiss possible effects of sampling bias. Nonetheless, we suggest that the
861 shallowness of Australian cratonic earthquakes, and their potential for lateral rupture
862 propagation at shallow depths through highly fractured cratonic crust is expected to
863 favour generation of higher *SRL:W* ratios and larger *MD* when compared to deeper, but
864 otherwise similarly-sized, crustal earthquakes in the global datasets (e.g., Wells and
865 Coppersmith (1994)). High *SRL:W* ratios are commonly observed in large earthquakes
866 (*Mw* > 7) (Weng and Ampuero, 2019) where the rupture width is limited by regional
867 brittle layer thickness. However, the shallowness and small rupture dimensions of the
868 Australian cratonic earthquakes studied here preclude the involvement of ductile
869 processes that limit the base of the rupture zone, such as enhanced viscous friction
870 (e.g., Schueller et al. (2005)).

871 The Kunayungku, Lake Surprise E and Petermann earthquakes (*Type 1*; Fig. 10)
872 have simple surface rupture geometries with few definable segments or trend
873 deviations (Fig. S3, Table S10), but widely variable $\Delta\sigma^s$ (Fig. 10A; Table S6). We
874 attribute this difference to the depth of the earthquake source. Our rupture width
875 estimates for the Kunayungku and Lake Surprise East earthquakes range from 9.8 –
876 11.6 km (Table S5), while published estimates extend from the surface to depths of >
877 6 km (Choy and Bowman, 1990) and up to 10 – 16 km (Bowman, 1991; Mohammadi
878 et al., 2019). InSAR inversion, CMT modelling and seismological analyses suggest

879 the Petermann earthquake was limited to the top ~4 km of the crust (Attanayake et al.,
880 2020; Hejrani and Tkalčić, 2019; Polcari et al., 2018). The frictional strength of fault
881 rocks in the shallow crust (< 5 km) in cratonic areas is proposed to be much lower
882 than deeper equivalents (Bamford, 1976; Denham et al., 1980), and thus otherwise
883 equivalent ruptures channelled along highly anisotropic crustal weak zones (*Type 1*)
884 that extend to greater depths are hypothesized to have larger $\Delta\sigma^s$ (Fig. 10).

885 We further speculate that increasing cratonic crustal strength with depth may
886 inhibit downward rupture propagation via increasing fault friction and decreasing
887 fracture continuity, whilst imposing a discernible effect on spectra of co-seismic slip
888 distributions (Fig. 5B). For many earthquakes (e.g., Calingiri, Petermann) we find high
889 energy concentrations at short wavelengths (1 to 5 km; Fig. 5) that are comparable with
890 rupture widths. We envisage the rupture process to involve progressive energy bursts of
891 propagating fractures with dimensions (e.g. diameters) set by the down-dip rupture
892 width; these fractures coalesce to impart higher frequency displacement variations that
893 are manifested as embedded shapes within the gross rupture profiles. These signals
894 would be more discernible in shallower earthquakes and more attenuated in deeper
895 earthquakes with smaller *SRL:W* ratios (e.g., Pukatja, Lake Surprise W).

896 This hypothesis is not incompatible with the large range of stress drops and rupture
897 displacement shapes we observe in shallow cratonic earthquakes, as aspects such as
898 co-seismic slip and rupture length could be highly dependent on shallow (< 5 km)
899 variations in crustal structure, lithology, and other factors whilst still adhering to our
900 hypothesis of depth-limited behaviour. The rupture of depth limited shallow

901 earthquakes may be comparably less constrained from propagating laterally due to the
902 presence of lithologic and structural heterogeneities that could enhance co-seismic
903 rupture growth (Attanayake et al., 2020). Just as the lateral dimension of fault
904 step-overs is important in limiting the size and mechanics of laterally propagating
905 ruptures (Wesnousky, 2006), perhaps variations in the strength (e.g., Mooney et al.
906 (2012)) and stress distributions in cratonic crust favour depth partitioning of
907 earthquakes with limited rupture widths. Our hypothesis also does not preclude the
908 occurrence of deep cratonic earthquakes, such as the 1989 magnitude 5.6 Uluru
909 earthquake (hypocentre depth = 31 km; Michael-Leiba et al. (1994)). Rather, we
910 suggest the strength and strongly segmented nature of fractures in cratonic lithosphere
911 could suppress upward propagation of deep earthquakes and downward propagation of
912 shallow earthquakes, and thereby potentially limit earthquake maximum M_w in cratons
913 (e.g., Mooney et al. (2012)).

914 **Implications for seismic hazard: PFDHA inputs**

915 The principal aim of Probabilistic Fault Displacement Hazard Analysis (PFDHA)
916 is to evaluate the potential for ground surface displacements of varying amounts, and
917 across varying time-scales, associated with seismogenic fault rupture (Moss and Ross,
918 2011; Youngs et al., 2003). Empirical distributions for *SRL*, *MD*, *AD*, spatial variability
919 of slip, and other statistical parameters are essential inputs into PFDHA calculations,
920 which include probabilities of surface rupture at different *Mw* and slip exceedance
921 distributions (Moss and Ross, 2011).

922 Figure 11A presents a new surface rupture probability curve for Australian cratonic
923 earthquakes and compares this curve to prior curves from global regressions (Moss and
924 Ross, 2011). Australian earthquake data was obtained for the period 1 January 1900 to
925 21 October 2020 from Geoscience Australia's Earthquake Catalogue
926 (https://earthquakes.ga.gov.au/). We note that this earthquake catalogue does not
927 include the revised M_W estimates from the 2018 National Seismic Hazard Assessment
928 (NSHA18) (Allen et al., 2018) from which our surface rupture M_W values are sourced.
929 However, the NSHA18 catalogue only extends to 2017 and excludes the Lake Muir
930 earthquake. The earthquake catalogue was restricted to onshore Precambrian
931 non-extended crust only (Fig. 1). We apply magnitude completeness cutoffs based on
932 the Australian continent M_C estimates of Allen et al. (2018) (M_C 6.5 > 1920; M_C 6.0 >
933 1920; M_C 4.5 > 1960; M_C 4.0 > 1970).
934 The percent of all earthquakes in each 0.1 M_w increment that caused surface rupture
935 are used as point data and fit by a regression curve with the logistic function following
936 the method of Moss and Ross (2011). Six of nine Australian SCR earthquakes in this
937 period with $M_w \geq 6.0$ generated surface ruptures and thus the probability of surface
938 rupture increases steeply over the $6.0 \leq M_w \geq 6.5$ interval. Termination of the Australian
939 SCR probability curve below 1.0 and at values of M_w > 6.6 is intended to reflect
940 epistemic uncertainty pertaining to the short historical seismologic record. Given the
941 diverse nature of the reverse fault and Australian SCR curves, PFDHA could consider
942 implementation of a logic tree weighted approach amongst these functions, depending
943 upon the geological-seismological inputs and the desired conservativity of the analysis.

944 As many deeper earthquakes in areas of enhanced sedimentary thickness contribute to
945 the global regression, we favor weighting towards the SCR Oz curve (0.6 to 0.7) in
946 Australian bedrock terrains.

947 Figure 11B compares observed *AD* and *MD* for the Australian earthquakes against
948 modelled *AD* and *MD* derived from regressions in the preeminent PFDHA framework
949 used to evaluate reverse faults (Moss and Ross (2011); equations in Fig. 11 caption).
950 Almost all Australia earthquakes have observed *AD* within ± 30% of the predicted *AD*
951 from Moss and Ross (2011) with the exception of the low slip, low stress drop
952 Petermann earthquake ('P', Fig. 11). However, 9 of 11 Australian earthquakes have
953 observed *MD* >> modelled *MD* (> +30% of predicted). We therefore calculate new *AD*
954 and *MD* to M_w linear regressions and present these in Figure 11B. These formulae could
955 be used or statistically preferred to other regressions (in a weighted logic tree content)
956 for PFDHAs in SCR bedrock regions.

957 In terms of displacement profiles, eight of eleven earthquakes (73%) have
958 observed *MD* in the central third of the rupture (Fig. 2) and seven of eleven earthquakes
959 (64%) have '*symmetric*' best-fitting functions (Fig. 3C; Table S2). Although a flat line
960 fit (displacement at any given point along the rupture is equal to *AD*) is not the preferred
961 shape for any events, it produces close results (i.e., *AD* ≈ modeled *MD*) to the best fit in
962 Petermann and Lake Surprise E. Incremental displacements along a specified fault in a
963 *Type 1* setting (Fig. 10) could thus be appropriately modelled using *AD* estimates
964 obtained from the scaling relationship in Fig. 11B. From the perspective of PFDHA
965 however, it is difficult to accurately forecast the shape and symmetry of surface rupture

displacement fields for future earthquakes across a diverse range of SCR settings. To resolve this, we normalize incremental displacements (*D*) against *AD* at fault positions (x) against *SRL* for all rupture types. The x axis is the rupture half length, with each rupture yielding two data points for each displacement increment. We fit a mean regression and 1σ error bounds to all data (Fig. 11C).

Fig. 11C shows *D* is ≤ *AD* within the first 10% of the *SRL* (measured from either rupture tip) and *D* ≥ *AD* within the middle 80% of the rupture (0.2 to 0.5). The highest values of *D* (i.e., > *AD*) and lowest uncertainty bounds are observed in the middle quintile of the rupture. *Type* 2 and 3 faults exhibit the largest variability along the rupture trace (i.e., *D/AD* > 1σ bounds). The largest 1σ incremental *D/AD* occur in the first 20% of the rupture length. PFDHA practitioners could consider the structural-geophysical setting type (Fig. 10) with these data (Fig. 11) to select conservative bounds for incremental PFDHA estimates depending upon the location of a site along a rupture trace. At the simplest level, the mean curve and 1σ bounds presented in Fig. 11C could represent a reasonable approximation of *D/AD* irrespective of geological setting.

As a final demonstration of how the results of this study could inform PFDHA, we show gamma probability distribution functions (PDFs) for *D / AD* at fixed values of x / *SRL* ranging from the first 5% of the surface rupture (*x / SRL* = 0.05) to the rupture mid-point (*x / SRL* = 0.5). PDFs shift to higher proportionate values of *D / AD* towards the rupture mid-point (i.e., *D* > *AD*), but retain strong probability distributions of *D* < *AD* at all locations.

CONCLUSIONS

1. *AD : MD* ratios range from 0.13 (Petermann earthquake) to 0.67 (Katanning) with a mean of 0.36 ± 0.14 (1σ). Of the 8 ruptures analyzed, 50% exhibit unilateral and 50% exhibit bilateral rupture directivity. If the observed and modelled positions of *MD* relative to *SRL* are combined, approximately 68% of earthquakes have *MD* in the middle third of the rupture and 16% each of the end thirds.
2. Surface co-seismic slip distributions for the studied earthquakes generally adhere to asymmetric triangular or elliptical shapes, but there is not a preferred shape for all events studied here. There are two prevailing endmember forms of co-seismic along-strike slip distribution: the low curvature to rectangular shape (e.g., Petermann; close to an elliptical shape) for earthquakes with a roughly straight and localized damage zone (*Type 1* structures) and the higher curvature shape (e.g., Meckering; close to a triangular shape) for earthquakes with complex segmented surface rupture geometries. The latter is proposed to originate from higher frictional stress on the fault plane relative to the former and may include intensive off-fault damage zones. Crustal structure plays an important role in rupture characteristics.
3. S-transform analysis on the residuals suggests that while basic shapes may be representative of the slip distributions there are significant contributions in the form of high spatial frequency (short-wavelength) signals that we attribute to factors that influence the rupture process, including stress concentrations

coincident with fault geometric complexities (e.g., stepovers or intersections) and depth controls on the rupture source (e.g., shallow earthquakes exhibit high frequency displacement variations with wavelengths similar to rupture width).

4. The higher value of *MD* and *SRL* in Australia compared to global examples may be attributed to the shallow earthquake hypocenters in the former data (mean 3.6 ± 1.9 km). Shallow earthquakes are expected to be more likely to have SRL ≈ subsurface rupture length, AD ≈ subsurface AD, and MD ≈ subsurface MD. Enhanced stress concentrations at geometrically compatible fault junctions (e.g., Marryat Creek) may further increase *MD*.

5. Surface rupture geometries are controlled by bedrock fabrics, which are mainly revealed by the TMI map. Of the total combined (summative) length of all surface ruptures (~148 km), we estimate between 133 km (90%) and 145 km (98%) aligns with geophysical structure in the host basement rocks. The host bedrock contains a dominant bedrock fabric that is structurally continuous in the scale of surface ruptures (e.g., 10's of km) and oriented perpendicular-to-high angle with respect to gravity gradients and S_{Hmax} tend to produce relatively simple and straight surface rupture (*Type 1*; e.g. Petermann). If the bedrock fabrics consists of intersected segments with variable orientations in the scale that is comparable to the surface rupture length, it tends to produce complex surface ruptures (*Type2* and *Type3*; e.g., Meckering and Cadoux). At the scale of this study, we are unable to determine whether TMI fabric geometries truly parallel rupture geometries in three dimensions, or are simply aligned in trace; if only the latter is true, TMI fabrics

may play more alternative roles in enhancing rupture propagation (e.g, fluid conduits) rather than simply providing zones of enhanced frictional weakness.

6. New $\Delta\sigma^s$ estimates are derived based on published estimates and three methods incorporating *W*, M_O, *AD*, and μ. The average stress drop for all earthquakes is 4.8 ± 2.8 (1 σ). $\Delta\sigma^s$ derived from ensemble models for the *Type 1* and *Type 3* earthquakes are close to or lower than the average from all earthquakes, and *Type 2* earthquakes has large variations in $\Delta\sigma^s$.

7. The rupture tip taper value at the termini is consistent with the result from global database and compliments existing data in slip mode. The asymmetry of displacement distribution and extremely steep rupture tip tapers are found to be affected by bedrock fabrics obliquely oriented with respect to the rupture strike.

8. The interaction between regional S_{Hmax}, intersecting segments, and the gravity gradient, increases surface rupture complexity (e.g., the Cadoux event). The segment length of a magnetic lineament that is normal to S_{Hmax} may set the limit of an earthquake surface rupture by intersecting other lineaments at low angle (< 45°) to the S_{Hmax}.

9. *MD* are commonly (8 of 11 earthquakes; 73%) located coincident with fault steps, bends, and/or high-angle fault intersections. S-transform analysis reveals that the spike-like high-frequency slip maxima also coincide with fault steps and junctions, suggesting concentrations of hierarchical fractal fault damage networks embedded within areas of geometric and kinematic incompatibility. The geometric compatibility or incompatibility of fault intersection zones provides a fruitful

avenue for future research. It is clear from this study that fault intersections should not be simply treated as converging areas where displacement tapers to net-zero slip in seismic hazard. In some cases, fault geometric complexities could be forecasted to have slip maxima; this is particularly important to consider in probabilistic fault displacement seismic hazard analyses for critical infrastructure.

10. The earthquakes in Australian SCRs have a higher surface rupture probability at $Mw > 5.7$ than predicted from prior reverse fault regression curves, necessitating consideration of additional surface rupture probability functions in PFDHA. Incremental surface displacements increase to approximately *AD* within the first 10% of the *SRL* (measured from either rupture tip) and $D \text{ is} \geq AD$ within the middle 80% of the rupture.

ACKNOWLEDGEMENTS

We would like to acknowledge the Noongar people of south-west Western Australia, the Warumungu people of Tennant Creek, and the Antakirinja, Yankunytjatjara, and Pitjantjatjara people of the Western Desert and APY lands in South Australia / Northern Territory, as the traditional custodians of the land on which all historic surface ruptures occurred, and where the data described in this paper were collected. This research was funded by the Australian Research Council through Discovery Grant #DP170103350 to M. Quigley. We acknowledge the support of Dan Clark and Trevor Allen from Geoscience Australia towards enhancing our knowledge

of Australian earthquakes. T. King received support from the David Hay Postgraduate Writing-Up Award (University of Melbourne). H. Yang received the Melbourne Research Scholarship, the Baragwanath Travel Scholarship and the Albert Shimmins Writing-Up Award from the University of Melbourne to assist in research development. Geophysical maps are produced by using the Generic Mapping Tools (GMT) package (Wessel et al., 2013).

REFERENCES

Adams, J., Wetmiller, R. J., Hasegawa, H. S., and Drysdale, J., 1991, The first surface faulting from a historical intraplate earthquake in North America: Nature, v. 352, no. 6336, p. 617-619.

Allen, T., Leonard, M., Ghasemi, H., and Gibson, G., 2018, The 2018 National Seismic Hazard Assesment: Earthquake epicentre catalogue (GA Record 2018/30). Geoscience Australia, Commonwealth of Australia, Canberra, ACT.

Allmann, B. P., and Shearer, P. M., 2009, Global variations of stress drop for moderate to large earthquakes: Journal of Geophysical Research-Solid Earth, v. 114, no. B1.

Andrews, D. J., 1989, Mechanics of Fault Junctions: Journal of Geophysical Research-Solid Earth and Planets, v. 94, no. B7, p. 9389-9397.

Attanayake, J., King, T. R., Quigley, M. C., Gibson, G., Clark, D., Jones, A. G., Brennand, S. L., and Sandiford, M., 2020, Rupture Characteristics and Bedrock Structural Control of the 2016 M w 6.0 Intraplate Earthquake in the

1095 Petermann Ranges, Australia: Bulletin of the Seismological Society of
1096 America.
1097 Bamford, W. E., 1976, Evolution of stresses in rock masses, as related to compressive
1098 strengths and plate tectonics: Investigation of Stress in Rock: Advances in
1099 Stress Measurement; Preprints of Papers, p. 63.
1100 Bowman, J. R., 1991, Geodetic Evidence for Conjugate Faulting during the 1988
1101 Tennant Creek, Australia Earthquake Sequence: Geophysical Journal
1102 International, v. 107, no. 1, p. 47-56.
1103 -, 1992, The 1988 Tennant Creek, Northern Territory, Earthquakes - a Synthesis:
1104 Australian Journal of Earth Sciences, v. 39, no. 5, p. 651-669.
1105 Brodsky, E. E., Gilchrist, J. J., Sagy, A., and Collettini, C., 2011, Faults smooth
1106 gradually as a function of slip: Earth and Planetary Science Letters, v. 302, no.
1107 1-2, p. 185-193.
1108 Brown, S. R., and Scholz, C. H., 1985, Broad Bandwidth Study of the Topography of
1109 Natural Rock Surfaces: Journal of Geophysical Research-Solid Earth and
1110 Planets, v. 90, no. B14, p. 2575-2582.
1111 Bürgmann, R., Pollard, D. D., and Martel, S. J., 1994, Slip distributions on faults:
1112 effects of stress gradients, inelastic deformation, heterogeneous host-rock
1113 stiffness, and fault interaction: Journal of Structural Geology, v. 16, no. 12, p.
1114 1675-1690.
1115 Cappa, F., Perrin, C., Manighetti, I., and Delor, E., 2014, Off-fault long-term damage:
1116 A condition to account for generic, triangular earthquake slip profiles:

1117 Geochemistry, Geophysics, Geosystems, v. 15, no. 4, p. 1476-1493.
1118 Choy, G. L., and Bowman, J. R., 1990, Rupture process of a multiple main shock
1119 sequence: analysis of teleseismic, local, and field observations of the Tennant
1120 Creek, Australia, earthquakes of January 22, 1988: Journal of Geophysical
1121 Research: Solid Earth, v. 95, no. B5, p. 6867-6882.
1122 Clark, D., Brennand, S., Brenn, G., Allen, T., Garthwaite, M., and Standen, S., 2019,
1123 The 2018 Lake Muir earthquake sequence, southwest Western Australia:
1124 rethinking Australian stable continental region earthquakes: Solid Earth.
1125 Clark, D., and McCue, K., 2003, Australian paleoseismology: towards a better basis
1126 for seismic hazard estimation: Annals of Geophysics, v. 46, no. 5, p.
1127 1087-1105.
1128 Clark, D., McPherson, A., Allen, T., and De Kool, M., 2014, Coseismic Surface
1129 Deformation Caused by the 23 March 2012 M-w 5.4 Ernabella (Pukatja)
1130 Earthquake, Central Australia: Implications for Fault Scaling Relations in
1131 Cratonic Settings: Bulletin of the Seismological Society of America, v. 104, no.
1132 1, p. 24-39.
1133 Clark, D., McPherson, A., and Van Dissen, R., 2012, Long-term behaviour of
1134 Australian stable continental region (SCR) faults: Tectonophysics, v. 566, p.
1135 1-30.
1136 Cowie, P. A., and Scholz, C. H., 1992a, Growth of Faults by Accumulation of Seismic
1137 Slip: Journal of Geophysical Research-Solid Earth, v. 97, no. B7, p.
1138 11085-11095.

-, 1992b, Physical Explanation for the Displacement Length Relationship of Faults Using a Post-Yield Fracture-Mechanics Model: Journal of Structural Geology, v. 14, no. 10, p. 1133-1148.

Crone, A. J., De Martini, P. M., Machette, M. N., Okumura, K., and Prescott, J. R., 2003, Paleoseismicity of two historically quiescent faults in Australia: Implications for fault behavior in stable continental regions: Bulletin of the Seismological Society of America, v. 93, no. 5, p. 1913-1934.

Dawson, J., Cummins, P., Tregoning, P., and Leonard, M., 2008, Shallow intraplate earthquakes in Western Australia observed by Interferometric Synthetic Aperture Radar: Journal of Geophysical Research-Solid Earth, v. 113, no. B11.

Denham, D., 1988, Australian seismicity-the puzzle of the not so stable continent: Seismological Research Letters, v. 59, no. 4, p. 235-240.

Denham, D., Alexander, L. G., Everingham, I. B., Gregson, P. J., Mccaffrey, R., and Enever, J. R., 1987, The 1979 Cadoux Earthquake and Intraplate Stress in Western-Australia: Australian Journal of Earth Sciences, v. 34, no. 4, p. 507-521.

Denham, D., Alexander, L. G., and Worotnicki, G., 1980, The stress field near the sites of the Meckering (1968) and Calingiri (1970) earthquakes, Western Australia: Tectonophysics, v. 67, no. 3-4, p. 283-317.

Dentith, M., Clark, D., and Featherstone, W., 2009, Aeromagnetic mapping of Precambrian geological structures that controlled the 1968 Meckering earthquake (Ms 6.8): Implications for intraplate seismicity in Western

Australia: Tectonophysics, v. 475, no. 3-4, p. 544-553.

Dentith, M. C., Dent, V. F., and Drummond, B. J., 2000, Deep crustal structure in the southwestern Yilgarn Craton, Western Australia: Tectonophysics, v. 325, no. 3-4, p. 227-255.

Dolan, J. F., and Haravitch, B. D., 2014, How well do surface slip measurements track slip at depth in large strike-slip earthquakes? The importance of fault structural maturity in controlling on-fault slip versus off-fault surface deformation: Earth and Planetary Science Letters, v. 388, p. 38-47.

Elliott, A. J., Dolan, J. F., and Oglesby, D. D., 2009, Evidence from coseismic slip gradients for dynamic control on rupture propagation and arrest through stepovers: Journal of Geophysical Research-Solid Earth, v. 114, no. B2.

Frankel, A., 1991, High-frequency spectral falloff of earthquakes, fractal dimension of complex rupture, b value, and the scaling of strength on faults: Journal of Geophysical Research: Solid Earth, v. 96, no. B4, p. 6291-6302.

Gabrielov, A., Keilis-Borok, V., and Jackson, D. D., 1996, Geometric incompatibility in a fault system: Proc Natl Acad Sci U S A, v. 93, no. 9, p. 3838-3842.

Gold, R. D., Reitman, N. G., Briggs, R. W., Barnhart, W. D., Hayes, G. P., and Wilson, E., 2015, On-and off-fault deformation associated with the September 2013 Mw 7.7 Balochistan earthquake: Implications for geologic slip rate measurements: Tectonophysics, v. 660, p. 65-78.

Gordon, F. R., and Lewis, J. D., 1980, The Meckering and Calingiri earthquakes October 1968 and March 1970.

Griffith, W. A., Di Toro, G., Pennacchioni, G., Pollard, D. D., and Nielsen, S., 2009, Static stress drop associated with brittle slip events on exhumed faults: Journal of Geophysical Research: Solid Earth, v. 114, no. B2.

Haeussler, P. J., Schwartz, D. P., Dawson, T. E., Stenner, H. D., Lienkaemper, J. J., Sherrod, B., Cinti, F. R., Montone, P., Craw, P. A., Crone, A. J., and Personius, S. F., 2004, Surface rupture and slip distribution of the Denali and Totschunda faults in the 3 November 2002 M 7.9 earthquake, Alaska: Bulletin of the Seismological Society of America, v. 94, no. 6, p. S23-S52.

Hejrani, B., and Tkalčić, H., 2019, The 20 May 2016 Petermann Ranges earthquake: centroid location, magnitude and focal mechanism from full waveform modelling: Australian Journal of Earth Sciences, v. 66, no. 1, p. 37-45.

Huang, Y., Ellsworth, W. L., and Beroza, G. C., 2017, Stress drops of induced and tectonic earthquakes in the central United States are indistinguishable: Sci Adv, v. 3, no. 8, p. e1700772.

Johnston, A., and Donnellan, N., 2001, Tennant Creek 1:250 000 Integrated Interpretation of Geophysics and Mapped Geology: Northern Territory Geological Survey, Alice Springs, Australia, scale 1:250 000.

Johnston, A. C., 1989, The seismicity of 'stable continental interiors', Earthquakes at North-Atlantic passive margins: Neotectonics and postglacial rebound, Springer, p. 299-327.

Kaneko, Y., and Fialko, Y., 2011, Shallow slip deficit due to large strike-slip earthquakes in dynamic rupture simulations with elasto-plastic off-fault

response: Geophysical Journal International, v. 186, no. 3, p. 1389-1403.

King, G., 1983, The Accommodation of Large Strains in the Upper Lithosphere of the Earth and Other Solids by Self-Similar Fault Systems - the Geometrical Origin of B-Value: Pure and Applied Geophysics, v. 121, no. 5-6, p. 761-815.

King, T. R., Quigley, M., and Clark, D., 2019, Surface-Rupturing Historical Earthquakes in Australia and Their Environmental Effects: New Insights from Re-Analyses of Observational Data: Geosciences, v. 9, no. 10, p. 408.

King, T. R., Quigley, M. C., and Clark, D., 2018, Earthquake environmental effects produced by the Mw 6.1, 20th May 2016 Petermann earthquake, Australia: Tectonophysics, v. 747, p. 357-372.

Klinger, Y., 2010, Relation between continental strike-slip earthquake segmentation and thickness of the crust: Journal of Geophysical Research: Solid Earth, v. 115, no. B7.

Leonard, M., 2008, One hundred years of earthquake recording in Australia: Bulletin of the Seismological Society of America, v. 98, no. 3, p. 1458-1470.

-, 2010, Earthquake Fault Scaling: Self-Consistent Relating of Rupture Length, Width, Average Displacement, and Moment Release: Bulletin of the Seismological Society of America, v. 100, no. 5a, p. 1971-1988.

Leonard, M., Burbidge, D., Allen, T., Robinson, D., McPherson, A., Clark, D., and Collins, C., 2014, The challenges of probabilistic seismic-hazard assessment in stable continental interiors: An Australian example: Bulletin of the Seismological Society of America, v. 104, no. 6, p. 3008-3028.

Lewis, J. D., Daetwyler, N. A., Bunting, J. A., and Moncrieff, J. S., 1981, The Cadoux earthquake, Western Australia: Geol. Surv. Rept, v. 11, p. 133.

Madariaga, R., 1977, Implications of stress-drop models of earthquakes for the inversion of stress drop from seismic observations, Stress in the Earth, Springer, p. 301-316.

Mai, P. M., and Beroza, G. C., 2002, A spatial random field model to characterize complexity in earthquake slip: Journal of Geophysical Research-Solid Earth, v. 107, no. B11, p. ESE 10-11-ESE 10-21.

Manighetti, I., King, G., and Sammis, C. G., 2004, The role of off-fault damage in the evolution of normal faults: Earth and Planetary Science Letters, v. 217, no. 3-4, p. 399-408.

Manighetti, I., Zigone, D., Campillo, M., and Cotton, F., 2009, Self-similarity of the largest-scale segmentation of the faults: Implications for earthquake behavior: Earth and Planetary Science Letters, v. 288, no. 3-4, p. 370-381.

McCue, K., Barlow, B. C., Denham, D., Jones, T., Gibson, G., and Michael-Leiba, M., 1987, Another chip off the old Australian block: Eos, Transactions American Geophysical Union, v. 68, no. 26, p. 609-612.

McGill, S. F., and Rubin, C. M., 1999, Surficial slip distribution on the central Emerson fault during the June 28, 1992, Landers earthquake, California: Journal of Geophysical Research-Solid Earth, v. 104, no. B3, p. 4811-4833.

Michael-Leiba, M., Love, D., McCue, K., and Gibson, G., 1994, The Uluru (Ayers Rock), Australia, earthquake of 28 May 1989: Bulletin of the Seismological

Society of America, v. 84, no. 1, p. 209-214.

Mohammadi, H., Quigley, M., Steacy, S., and Duffy, B., 2019, Effects of source model variations on Coulomb stress analyses of a multi-fault intraplate earthquake sequence: Tectonophysics, v. 766, p. 151-166.

Mooney, W. D., Ritsema, J., and Hwang, Y. K., 2012, Crustal seismicity and the earthquake catalog maximum moment magnitude (Mcmax) in stable continental regions (SCRs): Correlation with the seismic velocity of the lithosphere: Earth and planetary science letters, v. 357, p. 78-83.

Moss, R. E. S., and Ross, Z. E., 2011, Probabilistic Fault Displacement Hazard Analysis for Reverse Faults: Bulletin of the Seismological Society of America, v. 101, no. 4, p. 1542-1553.

Oglesby, D., 2008, Rupture termination and jump on parallel offset faults: Bulletin of the Seismological Society of America, v. 98, no. 1, p. 440-447.

Oglesby, D. D., 2020, What Can Surface-Slip Distributions Tell Us about Fault Connectivity at Depth?: Bulletin of the Seismological Society of America.

Okubo, P. G., and Aki, K., 1987, Fractal geometry in the San Andreas fault system: Journal of Geophysical Research: Solid Earth, v. 92, no. B1, p. 345-355.

Perrin, C., Manighetti, I., Ampuero, J. P., Cappa, F., and Gaudemer, Y., 2016, Location of largest earthquake slip and fast rupture controlled by along-strike change in fault structural maturity due to fault growth: Journal of Geophysical Research: Solid Earth, v. 121, no. 5, p. 3666-3685.

Polcari, M., Albano, M., Atzori, S., Bignami, C., and Stramondo, S., 2018, The

causative fault of the 2016 Mwp 6.1 Petermann ranges intraplate earthquake (Central Australia) retrieved by C-and L-band InSAR data: Remote Sensing, v. 10, no. 8, p. 1311.

Power, W. L., and Tullis, T. E., 1991, Euclidean and Fractal Models for the Description of Rock Surface-Roughness: Journal of Geophysical Research-Solid Earth and Planets, v. 96, no. B1, p. 415-424.

Quigley, M., Mohammadi, H., and Duffy, B., 2017, Multi-fault earthquakes with kinematic and geometric rupture complexity: how common: INQUA Focus Group Earthquake Geology and Seismic Hazards.

Quigley, M., Van Dissen, R., Litchfield, N., Villamor, P., Duffy, B., Barrell, D., Furlong, K. P., Stahl, T., Bilderback, E., and Noble, D., 2012, Surface rupture during the 2010 Mw 7.1 Darfield (Canterbury) earthquake: Implications for fault rupture dynamics and seismic-hazard analysis: Geology, v. 40, no. 1, p. 55-58.

Rajabi, M., Tingay, M., Heidbach, O., Hillis, R., and Reynolds, S., 2017, The present-day stress field of Australia: Earth-Science Reviews, v. 168, p. 165-189.

Scholz, C. H., and Lawler, T. M., 2004, Slip tapers at the tips of faults and earthquake ruptures: Geophysical Research Letters, v. 31, no. 21.

Schueller, S., Gueydan, F., and Davy, P., 2005, Brittle-ductile coupling: Role of ductile viscosity on brittle fracturing: Geophysical Research Letters, v. 32, no. 10.

Segall, P., and Pollard, D. D., 1980, Mechanics of Discontinuous Faults: Journal of

Geophysical Research, v. 85, no. Nb8, p. 4337-4350.

Shen, Z. K., Sun, J. B., Zhang, P. Z., Wan, Y. G., Wang, M., Burgmann, R., Zeng, Y. H., Gan, W. J., Liao, H., and Wang, Q. L., 2009, Slip maxima at fault junctions and rupturing of barriers during the 2008 Wenchuan earthquake: Nature Geoscience, v. 2, no. 10, p. 718-724.

Starr, A. T., Slip in a crystal and rupture in a solid due to shear, *in* Proceedings Mathematical Proceedings of the Cambridge Philosophical Society1928, Volume 24, Cambridge University Press, p. 489-500.

Stirling, M., McVerry, G., Gerstenberger, M., Litchfield, N., Van Dissen, R., Berryman, K., Barnes, P., Wallace, L., Villamor, P., Langridge, R., Lamarche, G., Nodder, S., Reyners, M., Bradley, B., Rhoades, D., Smith, W., Nicol, A., Pettinga, J., Clark, K., and Jacobs, K., 2012, National Seismic Hazard Model for New Zealand: 2010 Update: Bulletin of the Seismological Society of America, v. 102, no. 4, p. 1514-1542.

Stockwell, R. G., Mansinha, L., and Lowe, R. P., 1996, Localization of the complex spectrum: The S transform: Ieee Transactions on Signal Processing, v. 44, no. 4, p. 998-1001.

Thingbaijam, K. K. S., and Mai, P. M., 2016, Evidence for Truncated Exponential Probability Distribution of Earthquake Slip: Bulletin of the Seismological Society of America, v. 106, no. 4, p. 1802-1816.

Wells, D. L., and Coppersmith, K. J., 1994, New Empirical Relationships among Magnitude, Rupture Length, Rupture Width, Rupture Area, and Surface

Displacement: Bulletin of the Seismological Society of America, v. 84, no. 4, p. 974-1002.

Weng, H. H., and Ampuero, J. P., 2019, The Dynamics of Elongated Earthquake Ruptures: Journal of Geophysical Research-Solid Earth, v. 124, no. 8, p. 8584-8610.

Weng, H. H., and Yang, H. F., 2017, Seismogenic width controls aspect ratios of earthquake ruptures: Geophysical Research Letters, v. 44, no. 6, p. 2725-2732.

Wesnousky, S. G., 2006, Predicting the endpoints of earthquake ruptures: Nature, v. 444, no. 7117, p. 358-360.

-, 2008, Displacement and geometrical characteristics of earthquake surface ruptures: Issues and implications for seismic-hazard analysis and the process of earthquake rupture: Bulletin of the Seismological Society of America, v. 98, no. 4, p. 1609-1632.

Wessel, P., Smith, W., Scharroo, R., Luis, J., and Wobbe, F., 2013, Generic mapping tools: improved version released: Eos, Transactions American Geophysical Union, v. 94, no. 45, p. 409-410.

Youngs, R. R., Arabasz, W. J., Anderson, R. E., Ramelli, A. R., Ake, J. P., Slemmons, D. B., McCalpin, J. P., Doser, D. I., Fridrich, C. J., Swan, F. H., Rogers, A. M., Yount, J. C., Anderson, L. W., Smith, K. D., Bruhn, R. L., Knuepfer, P. L. K., Smith, R. B., dePolo, C. M., O'Leary, D. W., Coppersmith, K. J., Pezzopane, S. K., Schwartz, D. P., Whitney, J. W., Olig, S. S., and Toro, G. R., 2003, A methodology for probabilistic fault displacement hazard analysis (PFDHA):

Earthquake Spectra, v. 19, no. 1, p. 191-219.

Zhao, S., and Muller, R. D., 2003, Three-dimensional finite-element modelling of the tectonic stress field in continental Australia: SPECIAL PAPERS-GEOLOGICAL SOCIETY OF AMERICA, v. 372, p. 71.

Zielke, O., Klinger, Y., and Arrowsmith, J. R., 2015, Fault slip and earthquake recurrence along strike-slip faults—Contributions of high-resolution geomorphic data: Tectonophysics, v. 638, p. 43-62.

Zinke, R., Hollingsworth, J., and Dolan, J. F., 2014, Surface slip and off-fault deformation patterns in the 2013 MW 7.7 B alochistan, P akistan earthquake: Implications for controls on the distribution of near-surface coseismic slip: Geochemistry, Geophysics, Geosystems, v. 15, no. 12, p. 5034-5050.

FIGURES

Figure 1. (A) Map of Australia showing sites of historic surface-rupturing earthquakes, geological provinces (Leonard et al., 2014), onshore historic earthquakes > 4.0 (1840 – 2017) (Allen et al., 2018), crustal stress trajectory (Rajabi et al., 2017), neotectonic features (http://pid.geoscience.gov.au/dataset/ga/74056) and seismic zones (Leonard, 2008). The four rectangular boxes mark four high seismicity zones in Australia. (B) Maps of surface rupture for each event, numbered chronologically. Dots demonstrate the position of original field measurements, and the color code notes the amount of net slip. Small red arrows note the location of slip maxima for each event. (C) Interpreted bedrock geology surrounding the Tennant Creek events. The ruptures are aligned with local structures. The legend is simplified to focus on the structures around the surface rupture, for more details refer to Johnston and Donnellan (2001). (D) The geometric complexity of rupture segmentation versus the magnitude. The surface-rupturing earthquakes (M_w > 5.5) in Australia are plotted against global compilations (Quigley et al. 2017). The bars denote segmentation ranges of multi-fault earthquakes based on all reported studies.

Figure 2. Best-fitting regression curves of different regular shapes to the 11 co-seismic displacement profiles in Australian SCRs. The events are ordered by rupture length. The distance to the start point is normalized to the rupture length, which is labeled after the name of each event in the title. The filled circles represent the resampled data points. The red color means the resampled point has no original observations within 200 m while the grey ones indicate the nearest interpolation distance is < 200 m. The central quintile (x = 0.4 – 0.6) and central third (x = 0.33 – 0.67) are represented by the faint blue and pink box, respectively. The location of the preferred range of seismic derived epicenters in each area are projected to fault plane. The epicenter ranges roughly mark the relative position of sources with respect to the central third of the profile. A range across the whole profile means we cannot put any preferred range for corresponding event according to the reported data and uncertainties. The black arrow marks the position of the slip maxima that has the high spatial frequency in net slip (abrupt rise and drop in few hundred meters) coincident with fault stepovers, blue star coincident with fault junctions. For the slip taper calculation, we first use the asymmetric triangular shape function, which may over smooth the slip profile where there are strong perturbations. We correct those taper angle calculations at ending segments. The thick blue lines are corrections for the rupture tip taper calculation for those ending segments. The rupture length (*L*):width (*W*) ratios and average displacement *(AD)* : maximum displacement *(MD)* ratios are reported for each event. Stress drops (in MPa) reported from the literature ('observed'; see text for

sources) and modelled from a logarithmic regression fit to per unit area data ('***modelled***'; see text for details) are: Pukatja (***3.7***), Katanning (20.5, ***9.0***), Calingiri (9.0, ***6.0***), Lake Muir (***3.3***), Lake Surprise West (13.0, ***9.5***), Kunayungku (5.8, ***3.8***), Marryat Creek (***1.5***), Lake Surprise East (8.6, ***5.9***), Petermann (2.2, ***2.7***), Cadoux (2.0, ***2.4***), Meckering (9.0, ***4.9***) (Table S1, S6).

Figure 3. Post-analysis of the fitting results of different shapes. (A) adjusted R^2 for each shape function regression of all events to evaluate the goodness of the fitting. The higher R^2, the better fitting result. (B) The root-mean-square error (RMSE) is normalized by the mean value of corresponding measurements. (C) Symmetry for each event. (D) The rupture tip taper for each event. The insert sketch illustrates the calculation of rupture tip taper, which is defined as the spatial slip gradient when it approaches the terminus. The marked grey area within two black lines shows 1σ perturbations of the data (exclude 4 outliers of value > 10^{-3}). The perturbation within two red dash lines are existing dataset for long (>30 – 100s km) ruptures of strike-slip or normal fault mechanisms (Scholz and Lawler, 2004). Data for each subplot are included in Table S2.

Figure 4. S-transform analyses for the residuals of the best-fitting regression curves for different shapes. The dominating spatial frequency is generally less than 5, but there are significant high-frequency signals for Calingiri (at x = ~1.3 km), Marryat Creek (at x = ~5 km), Lake Surprise East (at x = ~7 km), Petermann (at x = ~8 km), Cadoux (at x = ~14 km).

Figure 5. Averaging amplitude of the S-transform results versus the spatial frequency (A) and wavelength (B) over the whole domain for each event. (A) Only those spatial frequency lower than 10 are shown here as the averaging method would smooth out those high spatial frequency signals and the mean amplitude quickly decreases with spatial frequency after the dominating spatial frequency (i.e.,1-3), especially for the stacked case. (B) The spatial frequency is converted to the wavelength with the rupture length. The down-dip rupture width is noted for each event and is also marked with a red box in x-axis for those events with $SRL:W > 1$. The mean amplitude of the S-transform results generally decreases with the wavelength, but some events have large contributions from short-wavelength signals (< ~5 km), which are comparable with the down-dip rupture width for those relatively shallow events.

Figure 6. Comparison of the maximum slip (A) and rupture length (B) versus magnitude scaling relationship for thrust earthquakes between non-extended cratons in Australia and Ungava (Canada) and other areas (Moss and Ross, 2011; Wells and Coppersmith, 1994). The solid lines correspond to the linear regression results for the two groups. The value of slip maxima and rupture length in Australia is estimated to be higher than global comparatives.

Figure 7. Histograms of the co-seismic slip for the Peterman (A) and Meckering (B) earthquakes. The insert plot shows the complementary cumulative distribution function ($1 - F(u)$), which are fit by exponential functions (EX) and truncated exponential functions (TEX). The fitting result is measured by R^2. The Petermann earthquake demonstrates a near-critical behavior, while the Meckering earthquake a sub-critical behavior. u_h and u_c are the unknown rate parameters in regression. In the case of the truncated exponential function, u_t is the position where the probabilities start to deviate from an exponential trend.

Figure 8. (A) Total magnetic intensity map shows how lineaments affect the development of surface ruptures. The uninterpreted map is put adjacent to the interpreted map. Based on the regional S_{Hmax} orientation, the 11 events are divided into two groups: (1) the Petermann, Pukatja, Marryat Creek and Tennant Creek events with an average azimuth of 21º – 32º and (2) the Cadoux, Meckering, Calingiri, Katanning and Lake Muir events with an east-west oriented SHmax. The area in each sub-plot has the same scale of 0.6º × 0.6º. The Spl. in Meckering is short for the secondary Splinter rupture. (B) The sketch model illustrates how the orientation of SHmax orientation with respect to lineaments (weak zones) may affect the surface rupture complexity.

Figure 9. (A) Bouguer gravity anomaly (Unit: μm s^{-2}) contours overlying the shading map of magnetic lineaments. The surface ruptures are drawn with black lines and their names are labelled adjacent to the rupture. The black arrows show regionally averaged SHmax. The red thick lines overlying the gravity contour near the Petermann rupture mark the steps of the contours at the points P and P'.

Figure 10. Relationship between stress drop and fault orientation for *Type 1*, *2* and *3*. (A) Stress drop relative to M_W with each event categorized into *Type*. Uncertainties for each stress drop are calculated based on all stress drop estimates (Table S6). Dashed line and grey box indicate the average stress drop ± 1σ. (B) The cumulative percent of rupture length relative to S_{Hmax} for each event, and per *Type* (where 0° is S_{Hmax} perpendicular and 90° is S_{Hmax} parallel). The number of segments assigned to each rupture are taken from King et al. (2019) and detailed in Table S8 – 10 and Fig. S3. While some *Type 2* and *3* events have well aligned segments (i.e. perpendicular to S_{Hmax}), they generally have a larger range in orientations than *Type 1* events, which also have fewer segments.

1473 **Figure 11.** A) Probability of surface rupture for reverse (from Moss and Ross,
1474 2011), normal (from Youngs et al., 2003), all slip kinematic types (from Youngs et al.,
1475 2003) and Australia SCR earthquakes (SCR Oz; this study). Empirical distributions are
1476 fit using logistic regressions; the SCR Oz curve is a best fit to a two-period moving
1477 average. The probability for all reverse faulting events is significantly lower than that of
1478 normal and all slip types for equivalent M_w, however the SCR Oz probability is
1479 significantly higher for equivalent M_w. Reverse, normal, and all distributions are only
1480 valid in the range of $5.5 \leq M_w \leq 8.0$ and SCR Oz is valid only for $4.0 \leq M_w \leq 6.6$.
1481
1482 B) Predicted values for average *(AD)* and maximum *(MD)* surface rupture
1483 displacements from the equations of Moss and Ross *(2011)* plotted against the observed
1484 *AD* and *MD* from King et al. (2019) and this study. The Moss and Ross (2011)
1485 equations are: *LOG(AD) = 0.3244 * Mw - 2.2192* and *LOG (MD) = 0.5102 * Mw –*
1486 *3.1971*. The 1:1 line is flanked by ± 30% error bounds. Outlier datapoints are labeled in
1487 bold (*AD*) and italics (*MD*): P = Petermann, LSE = Lake Surprise East, LSW = Lake
1488 Surprise West, M= Meckering, LM= Lake Muir, Puk = Pukatja, Cal = Calingiri. New
1489 M_w-based regression fits for *AD* and *MD* based only on the Australian SCR data appear
1490 in the legend; given that 9 of 11 Australian earthquakes have observed *MD* >>
1491 modelled (Ross and Moss, 2011) *MD*, these new regressions may preferred for SCR
1492 PFDHA analyses.
1493
1494 C) Normalized displacement (discrete displacement / *AD*) for Australian SCR

earthquakes plotted as a function of rupture half length (x/L, where $x/L = 0$ is the rupture tip and $x/L = 0.5$ is the rupture mid-point).

D) Gamma distributions for spatial variability in *AD* at different normalized positions (most proximal to rupture tip, x = 0.05; rupture mid-point, x = 0.5). These distributions may be used to obtain an *AD* probability distribution for PFDHA at specific sites (e.g., Moss and Ross, 2011); intermediate positions along the fault will have intermediate profiles.

Figure 1

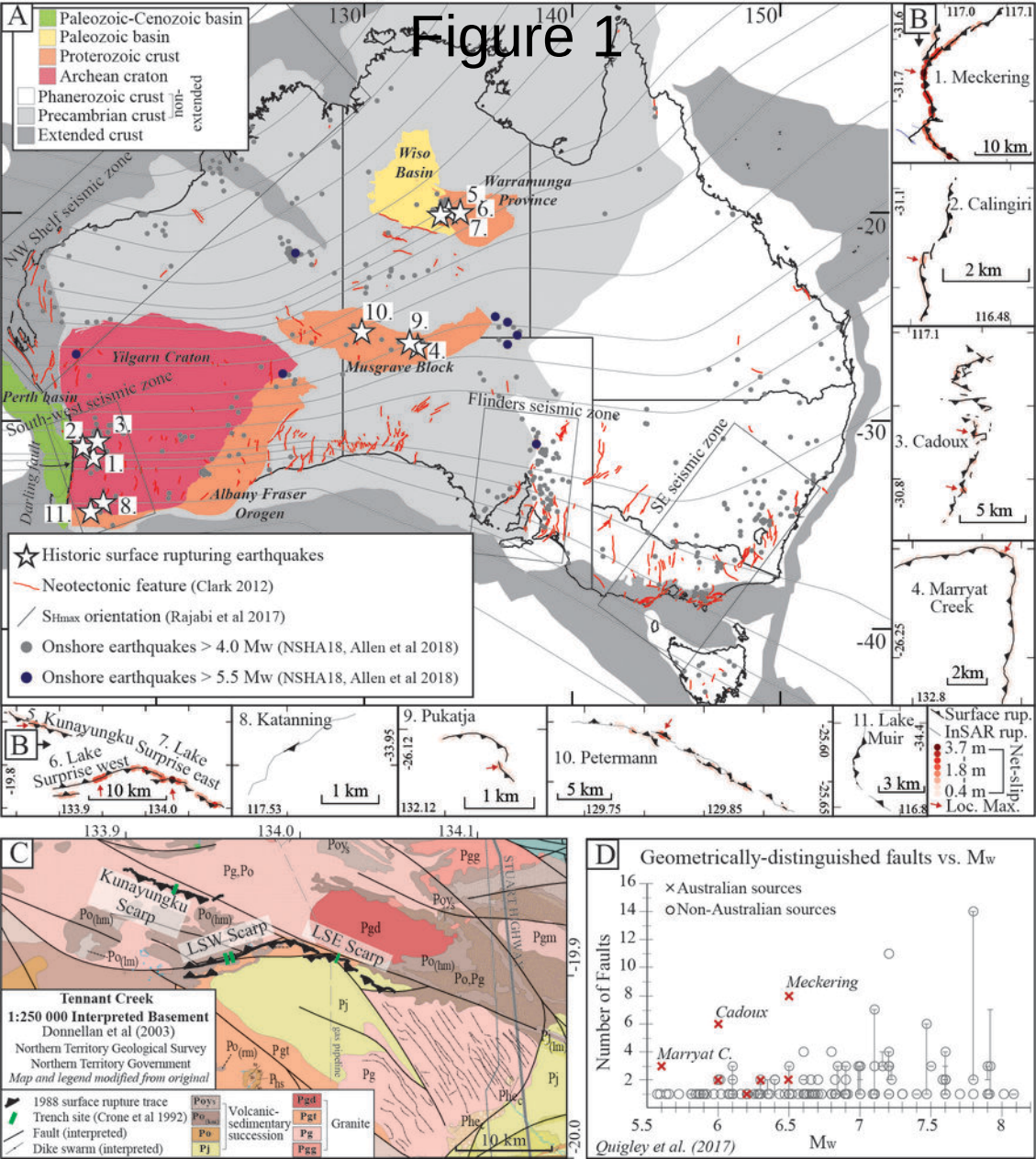
A
Paleozoic-Cenozoic basin
Paleozoic basin
Proterozoic crust
Archean craton
Phanerozoic crust
Precambrian crust
Extended crust
non-extended
NW Shelf seismic zone
Wiso Basin
Warramunga Province
Yilgarn Craton
Perth basin
South-west seismic zone
Darling fault
Musgrave Block
Albany Fraser Orogen
Flinders seismic zone
SE seismic zone
Historic surface rupturing earthquakes
Neotectonic feature (Clark 2012)
SHmax orientation (Rajabi et al 2017)
Onshore earthquakes > 4.0 Mw (NSHA18, Allen et al 2018)
Onshore earthquakes > 5.5 Mw (NSHA18, Allen et al 2018)
B
1. Meckering
10 km
2. Calingiri
2 km
3. Cadoux
5 km
4. Marryat Creek
2km
5. Kunayungku
6. Lake Surprise West
7. Lake Surprise east
10 km
8. Katanning
1 km
9. Pukatja
1 km
10. Petermann
5 km
11. Lake Muir
3 km
Surface rup.
InSAR rup.
Net-slip
3.7 m
1.8 m
0.4 m
Loc. Max.
C
Kunayungku Scarp
LSW Scarp
LSE Scarp
Stuart Highway
Tennant Creek
1:250 000 Interpreted Basement
Donnellan et al (2003)
Northern Territory Geological Survey
Northern Territory Government
Map and legend modified from original
1988 surface rupture trace
Trench site (Crone et al 1992)
Fault (interpreted)
Dike swarm (interpreted)
Volcanic-sedimentary succession
Granite
10 km
D
Geometrically-distinguished faults vs. Mw
Australian sources
Non-Australian sources
Meckering
Cadoux
Marryat C.
Number of Faults
Mw
Quigley et al. (2017)

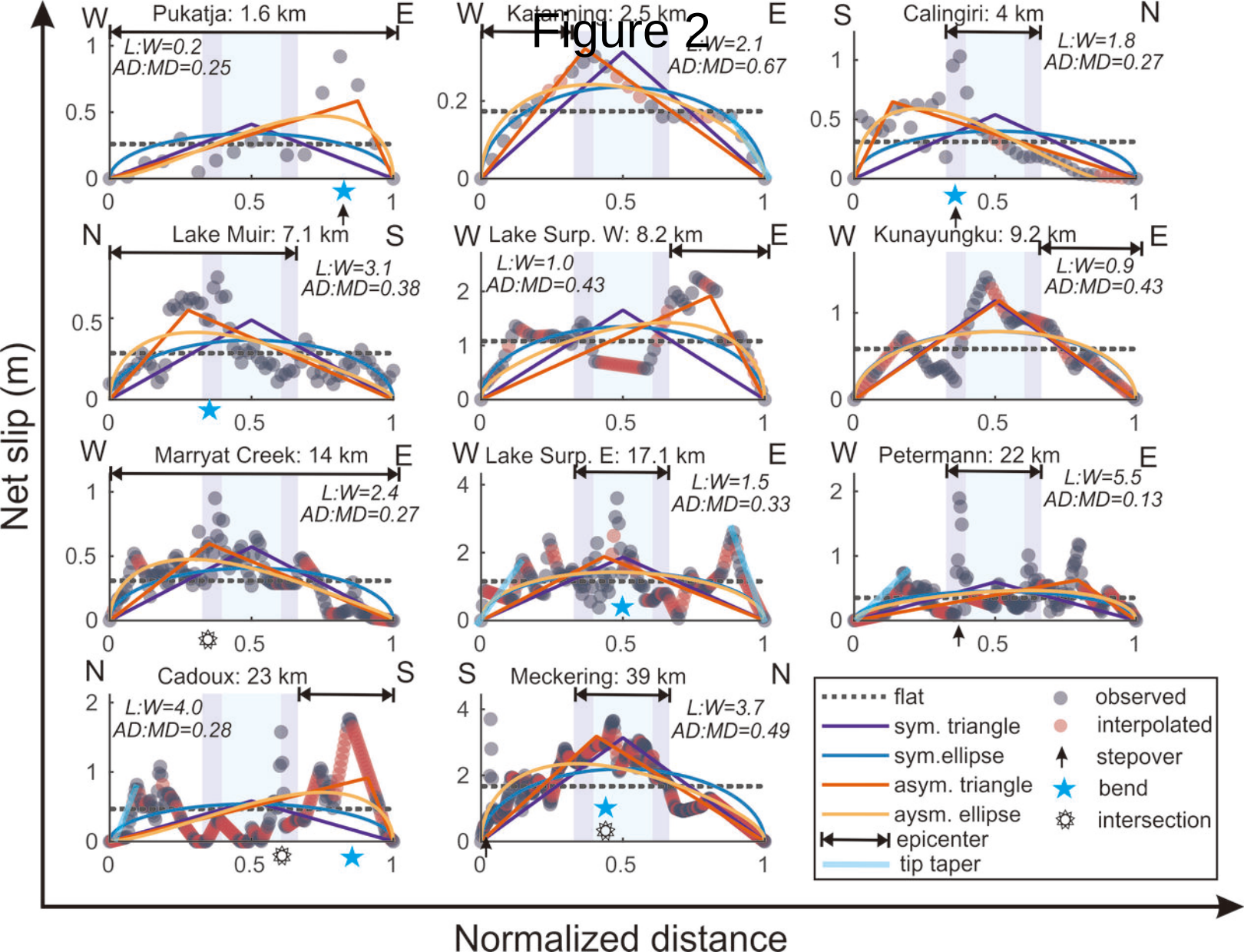
Figure 2
Pukatja: 1.6 km
L:W=0.2
AD:MD=0.25
Katanning: 2.5 km
L:W=2.1
AD:MD=0.67
Calingiri: 4 km
L:W=1.8
AD:MD=0.27
Lake Muir: 7.1 km
L:W=3.1
AD:MD=0.38
Lake Surp. W: 8.2 km
L:W=1.0
AD:MD=0.43
Kunayungku: 9.2 km
L:W=0.9
AD:MD=0.43
Marryat Creek: 14 km
L:W=2.4
AD:MD=0.27
Lake Surp. E: 17.1 km
L:W=1.5
AD:MD=0.33
Petermann: 22 km
L:W=5.5
AD:MD=0.13
Cadoux: 23 km
L:W=4.0
AD:MD=0.28
Meckering: 39 km
L:W=3.7
AD:MD=0.49
flat
sym. triangle
sym.ellipse
asym. triangle
aysm. ellipse
epicenter
tip taper
observed
interpolated
stepover
bend
intersection
Net slip (m)
Normalized distance

Figure 3

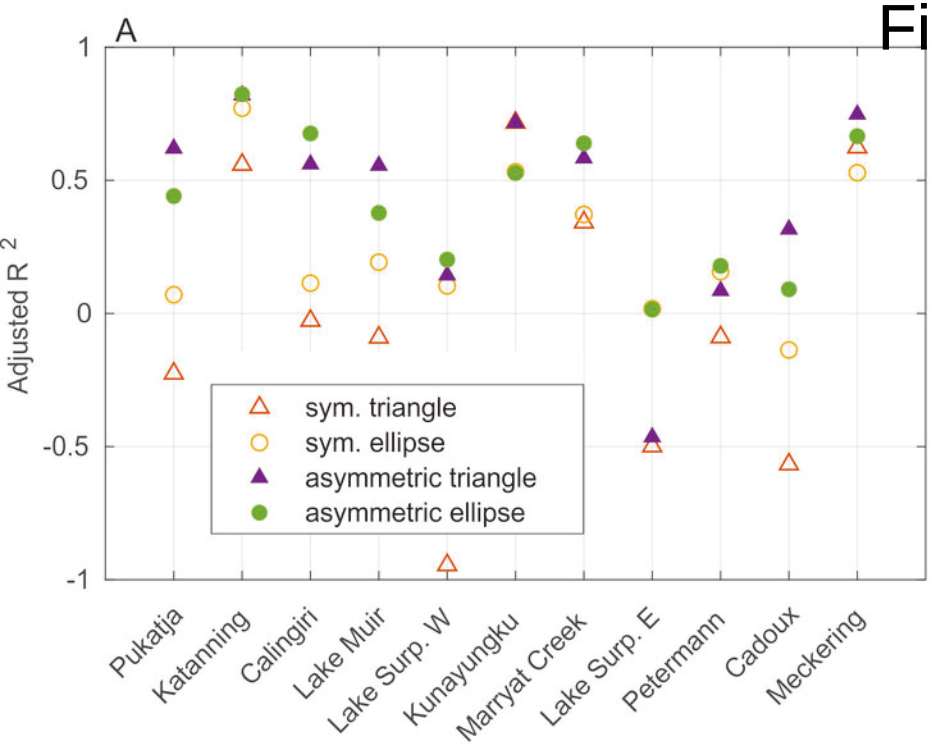
A
Adjusted R 2
sym. triangle
sym. ellipse
asymmetric triangle
asymmetric ellipse
Pukatja
Katanning
Calingiri
Lake Muir
Lake Surp. W
Kunayungku
Marryat Creek
Lake Surp. E
Petermann
Cadoux
Meckering

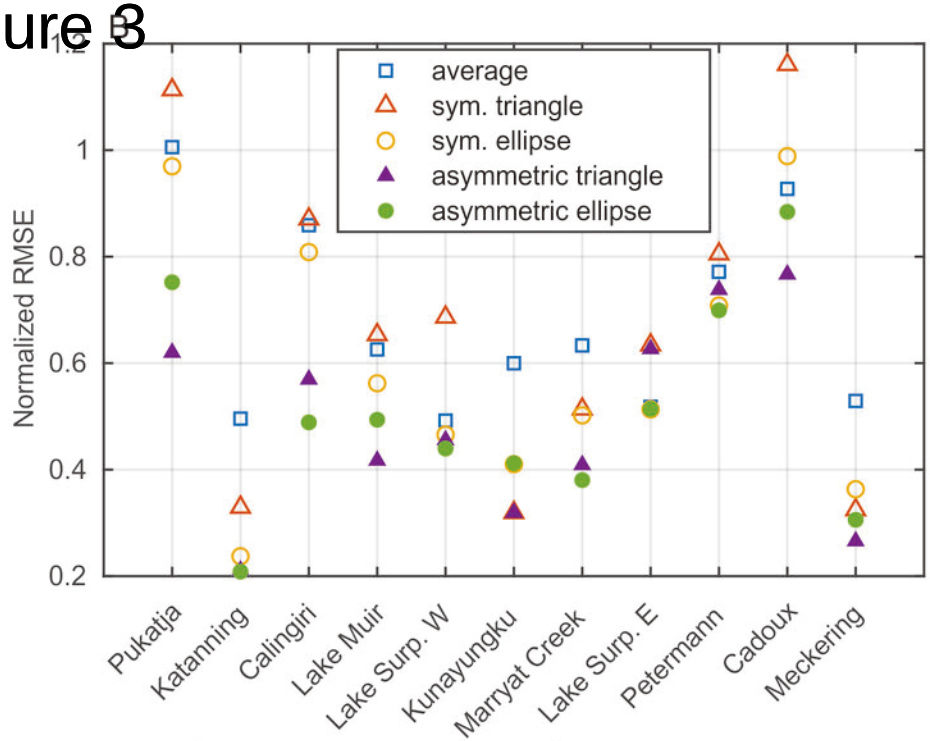
B
Normalized RMSE
average
sym. triangle
sym. ellipse
asymmetric triangle
asymmetric ellipse
Pukatja
Katanning
Calingiri
Lake Muir
Lake Surp. W
Kunayungku
Marryat Creek
Lake Surp. E
Petermann
Cadoux
Meckering

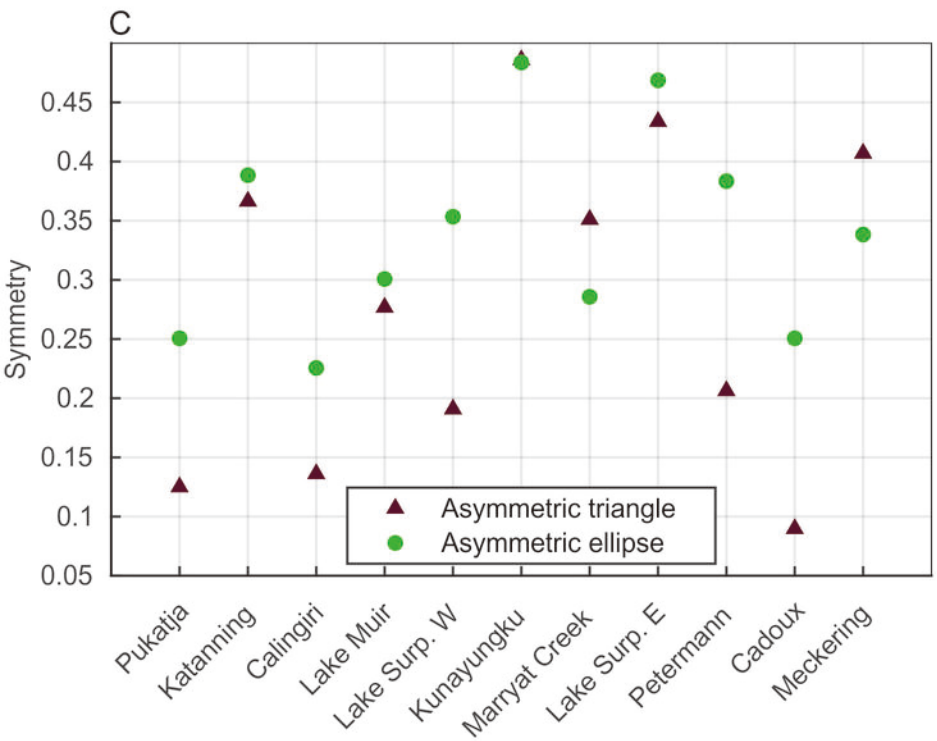
C
Symmetry
Asymmetric triangle
Asymmetric ellipse
Pukatja
Katanning
Calingiri
Lake Muir
Lake Surp. W
Kunayungku
Marryat Creek
Lake Surp. E
Petermann
Cadoux
Meckering

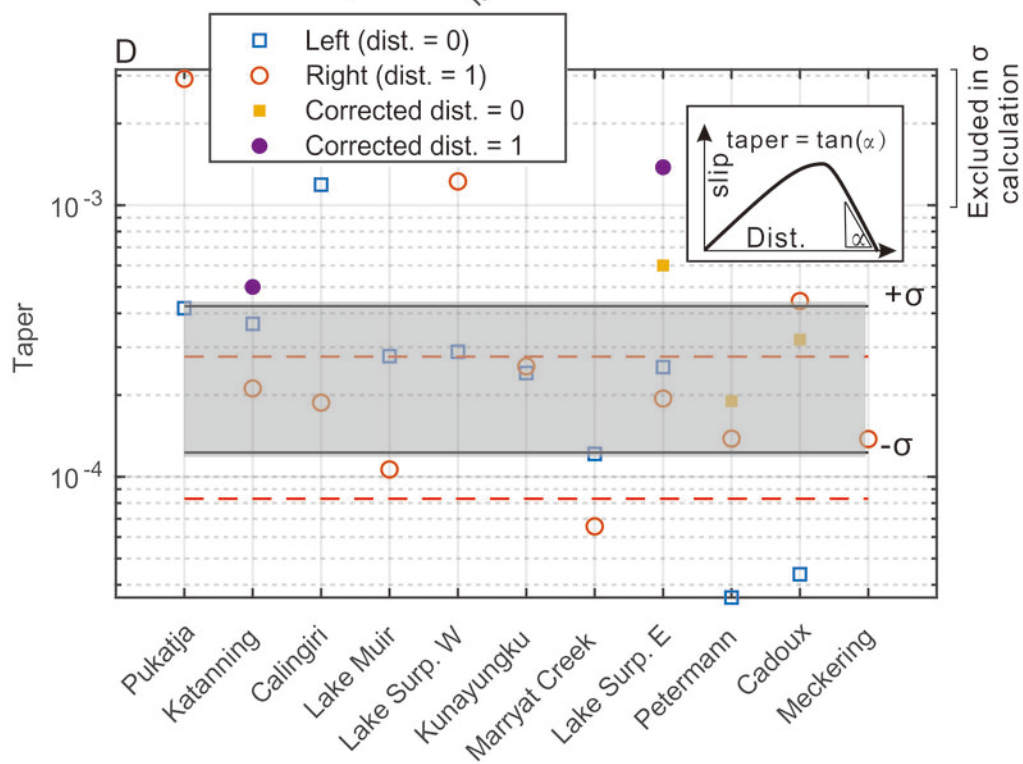
D
Taper
Left (dist. = 0)
Right (dist. = 1)
Corrected dist. = 0
Corrected dist. = 1
taper = tan(α)
slip
Dist.
+σ
-σ
Excluded in σ calculation
Pukatja
Katanning
Calingiri
Lake Muir
Lake Surp. W
Kunayungku
Marryat Creek
Lake Surp. E
Petermann
Cadoux
Meckering

Figure 4

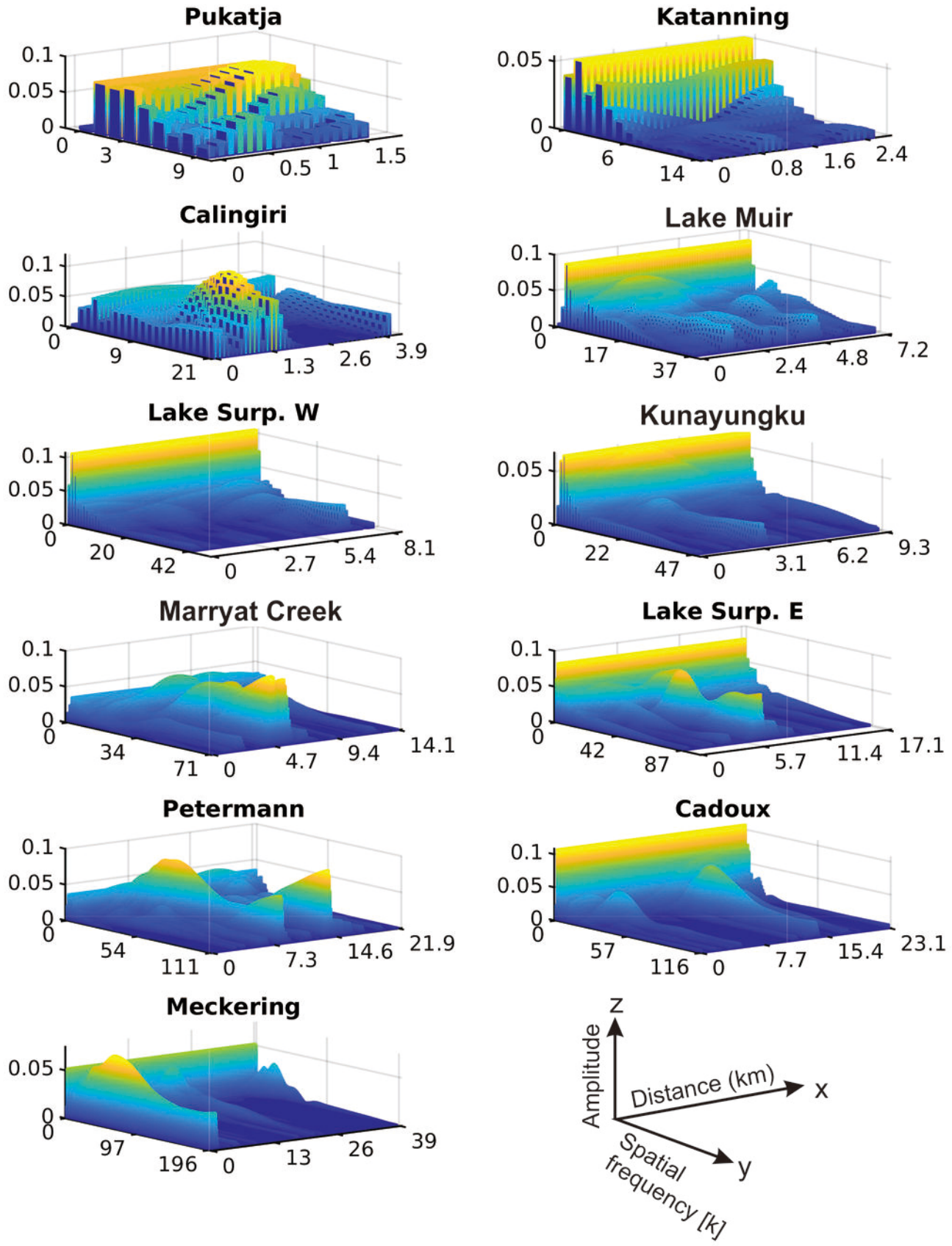
Pukatja
0.1
0.05
0
0
3
9
0
0.5
1
1.5
Katanning
0.05
0
0
6
14
0
0.8
1.6
2.4
Calingiri
0.1
0.05
0
0
9
21
0
1.3
2.6
3.9
Lake Muir
0.1
0.05
0
0
17
37
0
2.4
4.8
7.2
Lake Surp. W
0.1
0.05
0
0
20
42
0
2.7
5.4
8.1
Kunayungku
0.05
0
0
22
47
0
3.1
6.2
9.3
Marryat Creek
0.1
0.05
0
0
34
71
0
4.7
9.4
14.1
Lake Surp. E
0.1
0.05
0
0
42
87
0
5.7
11.4
17.1
Petermann
0.1
0.05
0
0
54
111
0
7.3
14.6
21.9
Cadoux
0.1
0.05
0
0
57
116
0
7.7
15.4
23.1
Meckering
0.05
0
0
97
196
0
13
26
39
Z
Amplitude
Distance (km)
x
Spatial
frequency [k]
y

Figure 5

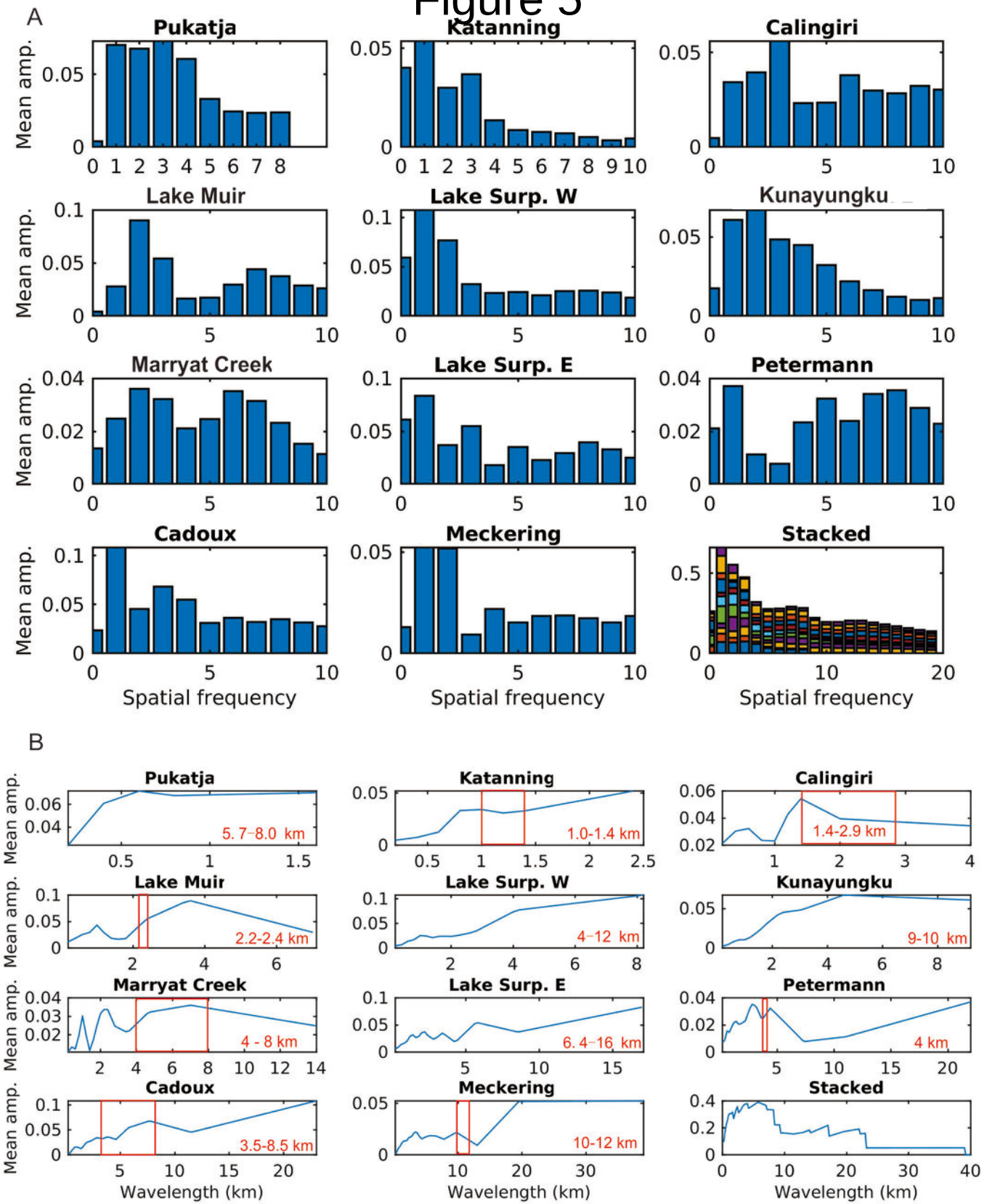
A
Pukatja
Katanning
Calingiri
Lake Muir
Lake Surp. W
Kunayungku
Marryat Creek
Lake Surp. E
Petermann
Cadoux
Meckering
Stacked
Mean amp.
Spatial frequency
B
Pukatja
5. 7–8.0 km
Katanning
1.0-1.4 km
Calingiri
1.4-2.9 km
Lake Muir
2.2-2.4 km
Lake Surp. W
4–12 km
Kunayungku
9-10 km
Marryat Creek
4 - 8 km
Lake Surp. E
6. 4–16 km
Petermann
4 km
Cadoux
3.5-8.5 km
Meckering
10-12 km
Stacked
Mean amp.
Wavelength (km)

Figure 6

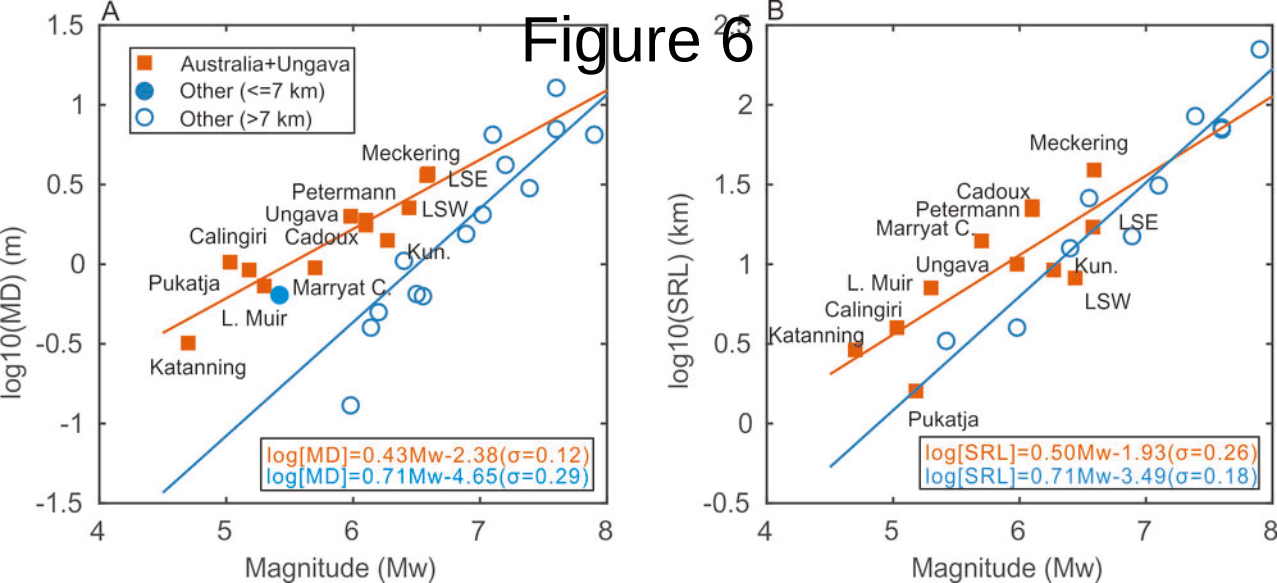
A
Australia+Ungava
Other (<=7 km)
Other (>7 km)
Meckering
LSE
Petermann
Ungava
LSW
Calingiri
Cadoux
Kun.
Pukatja
Marryat C.
L. Muir
Katanning
log[MD]=0.43Mw-2.38(σ=0.12)
log[MD]=0.71Mw-4.65(σ=0.29)
log10(MD) (m)
Magnitude (Mw)
B
Meckering
Cadoux
Petermann
Marryat C.
LSE
Ungava
Kun.
L. Muir
LSW
Calingiri
Katanning
Pukatja
log[SRL]=0.50Mw-1.93(σ=0.26)
log[SRL]=0.71Mw-3.49(σ=0.18)
log10(SRL) (km)
Magnitude (Mw)

Figure 7

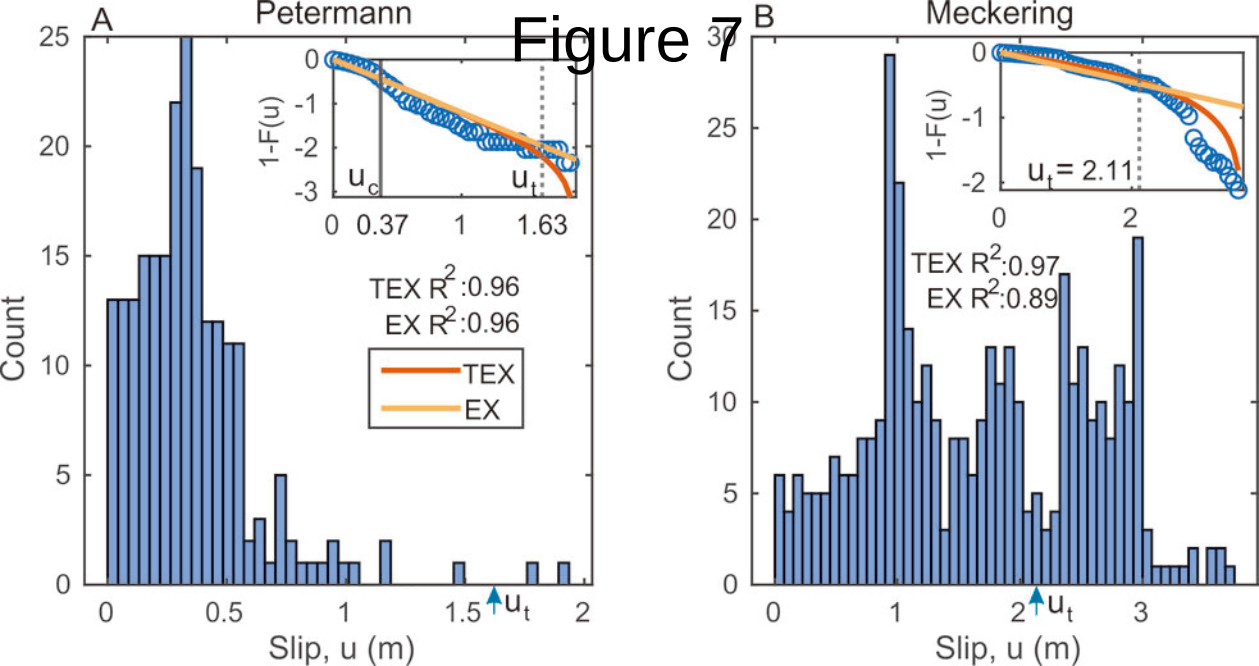
A
Petermann
Count
Slip, u (m)
1-F(u)
u_c
u_t
0.37
1.63
TEX R^2:0.96
EX R^2:0.96
TEX
EX
B
Meckering
u_t = 2.11
TEX R^2:0.97
EX R^2:0.89

Figure 8

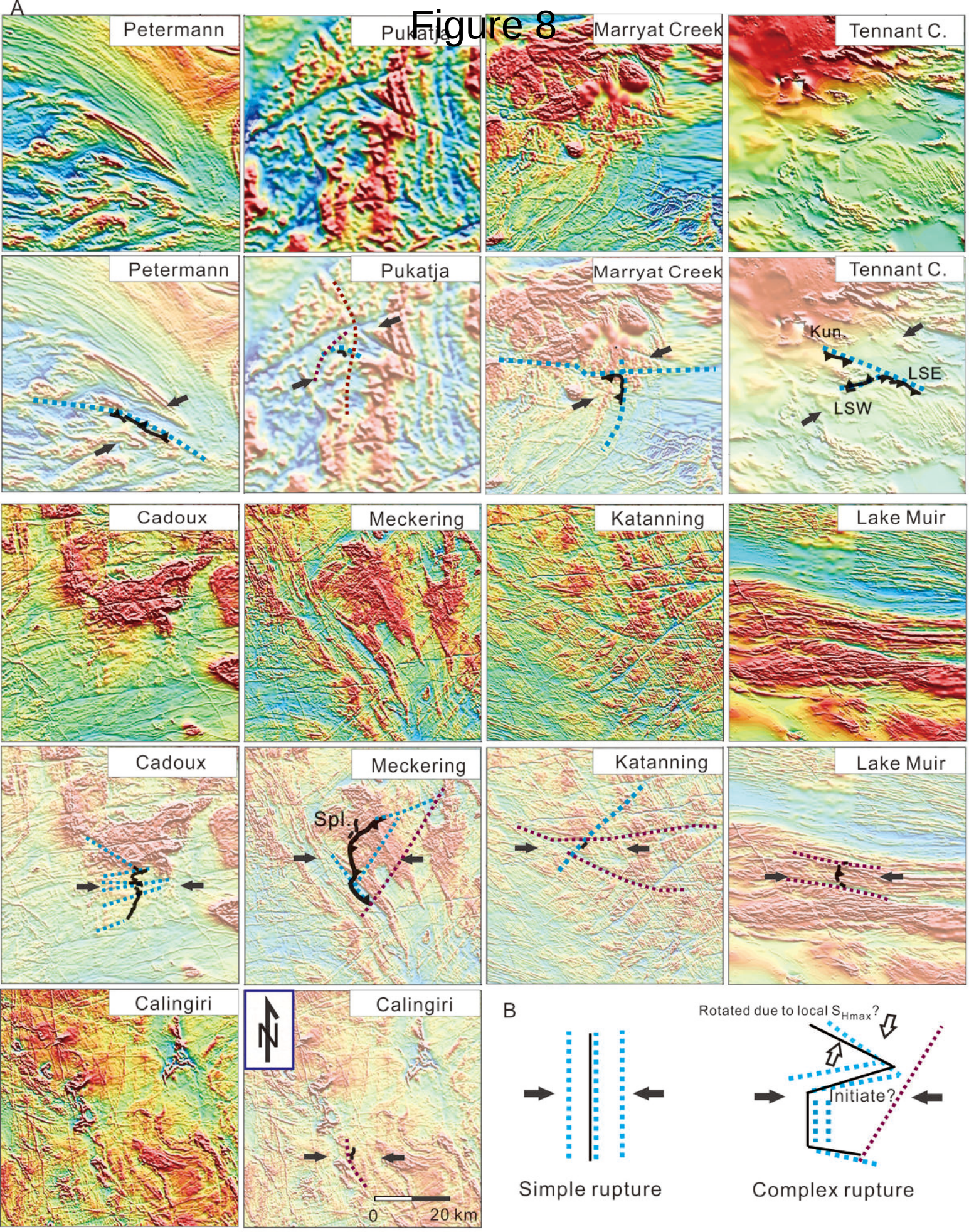
A
Petermann
Pukatja
Marryat Creek
Tennant C.
Petermann
Pukatja
Marryat Creek
Tennant C.
Kun.
LSE
LSW
Cadoux
Meckering
Katanning
Lake Muir
Cadoux
Meckering
Spl.
Katanning
Lake Muir
Calingiri
Calingiri
0
20 km
B
Simple rupture
Rotated due to local S_{Hmax}?
Initiate?
Complex rupture
nT
−800 −600 −400 −200 0 200
surface rupture
lineaments ruptured by earthquakes
lineaments as potential barriers
regional S_{Hmax}
locally rotated S_{Hmax}

Figure 9

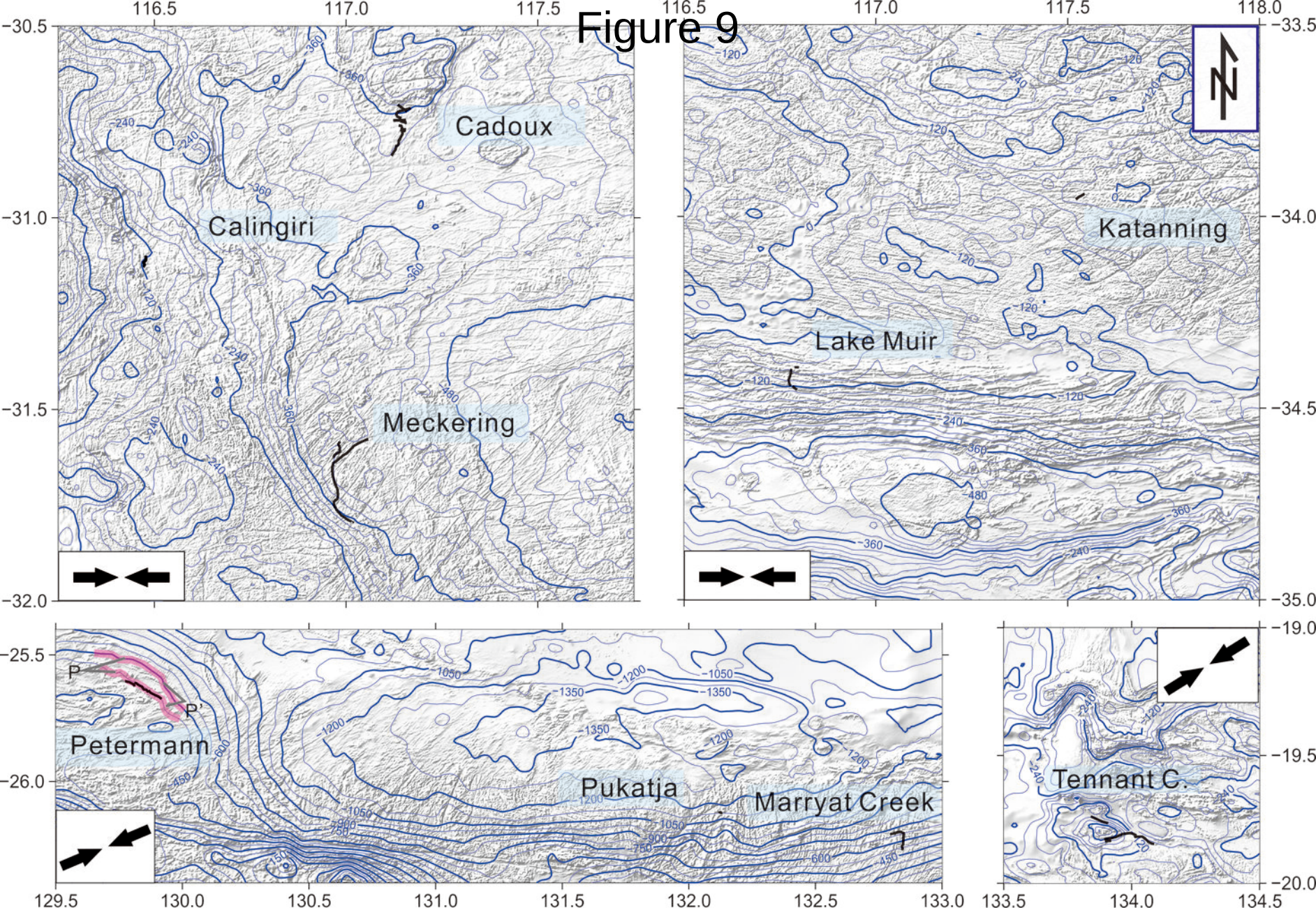
Cadoux
Calingiri
Meckering
Katanning
Lake Muir
Petermann
Pukatja
Marryat Creek
Tennant C.
P
P'
116.5
117.0
117.5
118.0
-30.5
-31.0
-31.5
-32.0
-33.5
-34.0
-34.5
-35.0
-25.5
-26.0
-19.0
-19.5
-20.0
129.5
130.0
130.5
131.0
131.5
132.0
132.5
133.0
133.5
134.0
134.5

Figure 10

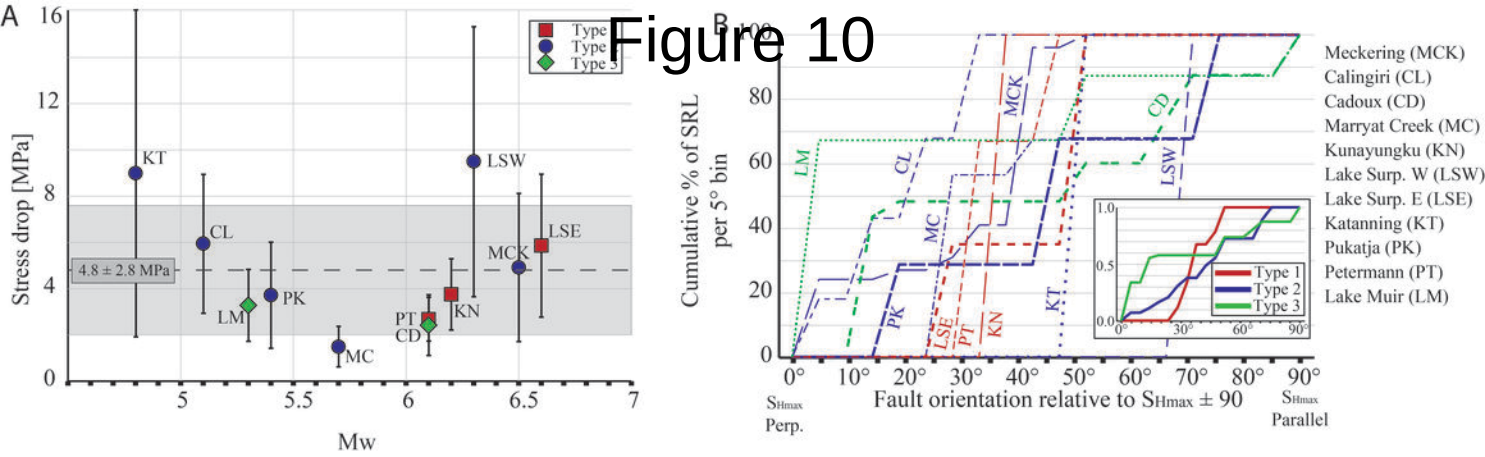
A
B
Stress drop [MPa]
Mw
Type 1
Type 2
Type 3
4.8 ± 2.8 MPa
KT
CL
LM
PK
PT
CD
MC
KN
LSW
MCK
LSE
Cumulative % of SRL per 5° bin
Fault orientation relative to SHmax ± 90
SHmax Perp.
SHmax Parallel
Meckering (MCK)
Calingiri (CL)
Cadoux (CD)
Marryat Creek (MC)
Kunayungku (KN)
Lake Surp. W (LSW)
Lake Surp. E (LSE)
Katanning (KT)
Pukatja (PK)
Petermann (PT)
Lake Muir (LM)

Figure 11

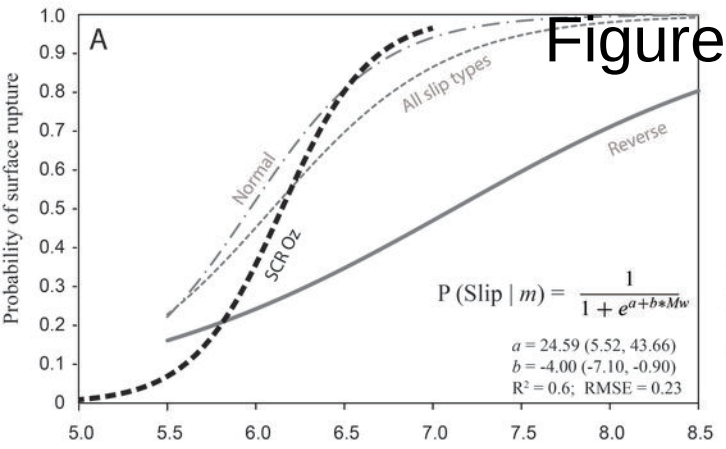
A
Probability of surface rupture
All slip types
Normal
Reverse
SCR Oz
P (Slip | m) = 1 / (1 + e^{a+b*Mw})
a = 24.59 (5.52, 43.66)
b = -4.00 (-7.10, -0.90)
R² = 0.6; RMSE = 0.23

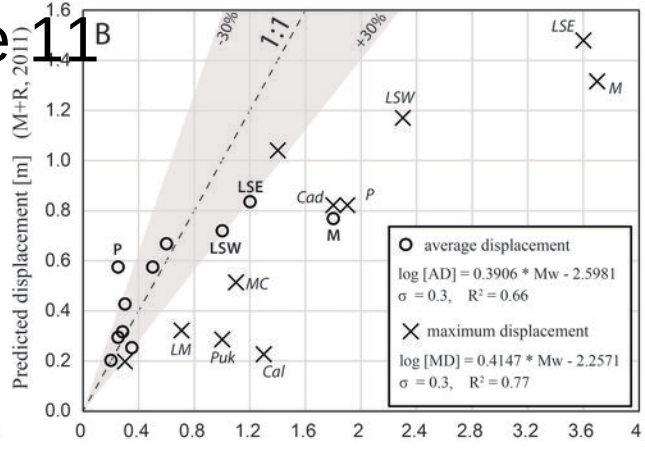
B
-30%
1:1
+30%
LSE
M
LSW
Cad
P
MC
LM
Puk
Cal
Predicted displacement [m] (M+R, 2011)
Observed displacement [m]
average displacement
log [AD] = 0.3906 * Mw - 2.5981
σ = 0.3, R² = 0.66
maximum displacement
log [MD] = 0.4147 * Mw - 2.2571
σ = 0.3, R² = 0.77

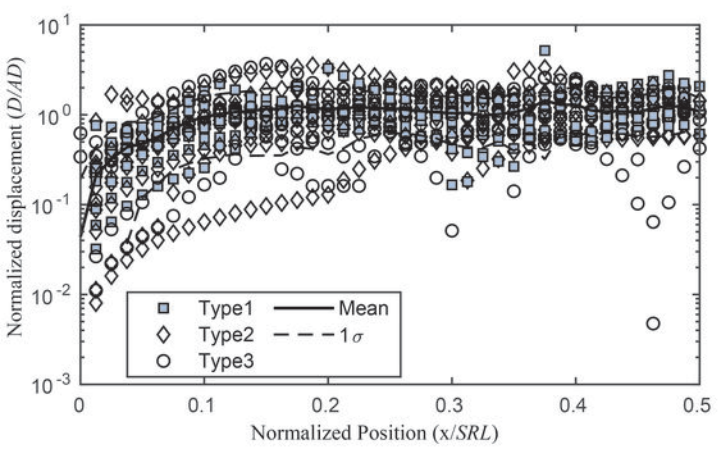
Normalized displacement (D/AD)
Type1
Type2
Type3
Mean
1σ
Normalized Position (x/SRL)

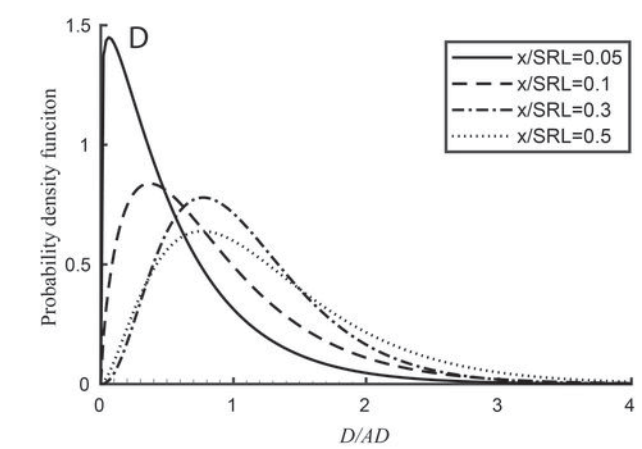
D
Probability density funciton
x/SRL=0.05
x/SRL=0.1
x/SRL=0.3
x/SRL=0.5
D/AD